Isogeometric analysis of 3D straight beam-type structures by Carrera Unified Formulation

Yang Yan [*], Erasmo Carrera [†], Alfonso Pagani [‡], Ibrahim Kaleel [§], Alberto Garcia de Miguel [¶]

Mul^2, Department of Mechanical and Aerospace Engineering, Politecnico di Torino, Corso Duca degli Abruzzi 24, 10129 Torino, Italy

Submitted to

Applied Mathematical Modelling

Author for correspondence:
Alfonso Pagani,
Department of Mechanical and Aerospace Engineering,
Politecnico di Torino,
Corso Duca degli Abruzzi 24,
10129 Torino, Italy,
tel: +39 011 090 6887,
fax: +39 011 090 6899,
e-mail: alfonso.pagani@polito.it

[*]Research Fellow, e-mail: yanyang864914630@126.com
[†]Professor of Aerospace Structures and Aeroelasticity, e-mail: erasmo.carrera@polito.it
[‡]Assistant Professor, e-mail: alfonso.pagani@polito.it
[§]Research Fellow, e-mail: ibrahim.kaleel@polito.it
[¶]Research Fellow, e-mail: alberto.garcia@polito.it

ABSTRACT

This paper applies the isogeometric analysis (IGA) based on unified one-dimensional (1D) models to study static, free vibration and dynamic responses of metallic and laminated composite straight beam structures. By employing the Carrera Unified Formulation (CUF), 3D displacement fields are expanded as 1D generalized displacement unknowns over the cross-section domain. 2D hierarchical Legendre expansions (HLE) are adopted in the local area for the refinement of cross-section kinematics. In contrast, B-spline functions are used to approximate 1D generalized displacement unknowns, satisfying the requirement of interelement high-order continuity. Consequently, IGA-based weak-form governing equations can be derived using the principle of virtual work and written in terms of fundamental nuclei, which are independent of the class and order of beam theory. Several geometrically linear analyses are conducted to address the enhanced capability of the proposed approach, which is prominent in the detection of shear stresses, higher-order modes and stress wave propagation problems. Besides, 3D-like behaviors can be captured by the present IGA-based CUF-HLE method with reduced computational costs compared with 3D finite element method (FEM) and FEM-based CUF-HLE method.

Keywords: Isogeometric analysis; Carrera Unified Formulation; Beam structures; B-spline functions; Hierarchical Legendre expansions

1 Introduction

Slender structures, known as beams, are vastly utilized as primary and secondary components in various engineering applications and fields, such as in aircraft wings in aerospace engineering, in girders of long-span bridges in civil engineering, and in gas pipelines in ocean engineering. During the period of their service, these structures are susceptible to endure a variety of external loads; e.g., dead loads, impact loads, and cyclic loads. A number of one-dimensional (1D) structural models have been developed for the optimal and safe design of beam structures. Despite this, the exact characterization of stress/strain fields and dynamic responses in these structural components still remains an open issue and more advanced simulation techniques are preferred and needed continuously in many industrial applications.

Euler-Bernoulli Beam Model (EBBM) [1] and Timoshenko Beam Model (TBM) [2] are two well-known classical beam theories. The former [3] assumed that the cross section remains perpendicular to the neutral layer after deformation, thus neglecting shear deformation effects. The latter relaxed the normality assumption of plane sections, leading to a constant shear distribution in the thickness direction. Boley [4] presented series solutions based on EBBM for the stresses and displacements of rectangular beams in the pure bending state. The results showed that EBBM is sufficiently accurate for thin beams. Various finite element models were introduced to study free vibration responses of Timoshenko beams by accounting for the shear deformation and rotary inertia [5–7]. Compared with EBBM, TBM is more suitable for handling the issue of thick beams and higher-order modes . However, a shear correction factor should be introduced to satisfy the stress-free conditions on the lateral surfaces. Further applications of EBBM and TBM in the mechanical analyses of thin-walled and composite beams can be founded in [8–10]. Although fruitful results are obtained using TBM, questions abound over the determination of the shear correction factor. In order to overcome the drawback of classical theories, several refined beam models have been proposed, including higher-order shear deformation theories (HSDT) [11–16], the generalized beam theory (GBT) [17–21], the warping function [22–26] and the variational asymptotic method (VAM) [27–29].

Although the aforementioned refined beam models can improve the numerical accuracy to some extent, some of them cannot address non-classical effects; e.g., torsion, warping and in-plane deformations at the same time. From this standpoint, the Carrera Unified Formulation (CUF) was introduced to solve mechanical problems of various beam structures in a unified manner. The basic idea of CUF is to degenerate any structural theories into generalized kinematics by means of arbitrary expansions of unknown variables, e.g., displacement or stress components. Initially, CUF was exploited for the development of plate and shell (2D) models [30] and extended to beam (1D) models [31]. Depending on the choice of the polynomials employed in the expansion, 1D CUF can be classified as follows: 1D CUF-TE (Taylor expansion), -LE (Lagrange expansion), -HLE (hierarchical Legendre expansion) and -CE (Chebyshev expansion). TE [32] and CE [33] define the cross-section kinematics in a global sense, thus enhancing the solutions through an increase of the polynomial order. In contrast, LE [34] and HLE [35] make use of discretizations of the cross-section domain, thus they represent the total surface exactly and can deal with thin-walled and composite sections more accurately. Besides, the addition of higher-order terms in LE requires the re-allocation of interpolation points and redefinition of the lower-order terms, leading to a cumbersome work in the pre-processing stage. On the other hand, HLE combines

the advantage of the hierarchy of the expansion order in TE and the local refinement of cross-section kinematics in LE, therefore they are more suitable for dealing with beam problems of arbitrarily complex geometric and material properties. 1D CUF models [33–37] were applied to the linear static and free vibration analysis of isotropic beams with arbitrary cross-section geometries. By comparing these results, 1D CUF-CE and -TE produced much closer solutions, which were less accurate than those predicted by 1D CUF-LE and -HLE with reference to 3D solid solutions over highly deformed zones. Similar mechanical problems of composite beams have also been conducted by these four 1D CUF models [33, 38–41], showing that the global deformations featured by the complicated coupling of the bending-shear-torsion due to the heterogeneity of the laminates can be perfectly detected with 10-100 times fewer degrees of freedom than 3D numerical results provided by commercial software tools.

It should be pointed out that, governing equations of 1D CUF can be solved by closed-form and numerical solutions. Closed-form solutions are represented by Navier-type [42–45] and Dynamic Stiffness Method (DSM) [46]. Although they are error-free mathematically, the former is confined to simply supported boundary conditions and the latter comes through the resolution of a nonlinear, transcendental eigenvalue problem. Numerical solutions can be distinguished as the strong-form and weak-form solutions. Classical C^0 Finite Element Method (FEM), as a member of weak-form solutions, provides the convenience to handle arbitrary geometries and loading conditions. Whereas quite dense mesh is needed in order to analyze the area of high-gradient stresses, capture higher-order modes and describe wave propagation with high-frequency components. Therefore, the development of efficient weak-form solutions is still appealing, which is the case of interest for this paper.

Isogeometric analysis (IGA), presented by Hughes et al. [47], has proven itself to be a useful tool in coping with an array of engineering problems in computational mechanics [48]. The core idea of IGA is to use B-splines or non-uniform rational B-splines (NURBS) describing geometrical information in computer-aided design (CAD) to approximate solution fields in FEM, bridging the existing gap between CAD and computer-aided engineering (CAE). This approach enables the mesh refinement process without interaction with the CAD system. Moreover, C^{p-1}-continuous B-spline or NURBS basis functions in IGA are superior to C^0-continuous Lagrange basis functions in FEM, leading to improved solutions without geometrical errors. Up to now, IGA has been widely employed to analyze the behavior of beam structures, with B-splines for straight beams and NURBS for curved beams. Kiendl et al. [49] established single-variable formulations for the Timoshenko beam problem based on IGA. Such novel formulations were completely locking-free and involved only half of degrees of freedom compared to standard Timoshenko formulations. Cottrell et al. [50, 51] developed the concept of IGA to structural vibration and wave propagation problems and investigated the effects of different mesh refinement strategies on the higher-order modes. Wen et al. [52] considered IGA for transient wave propagation problems with a robust implicit time integration scheme. Elastodynamic problems of beam structures subjected to moving vehicles were conducted by Van [53] using a NURBS-based formulation. The works above pay a special attention to the straight beam problems. NURBS-based IGA was introduced by Luu et al. [54] to investigate in-plane free vibrations of curved beams and rings with the variable curvature. Maurin et al. [55] proposed a rotation-free isogeometric framework to solve static and dynamic problems of planar beam structures. Furthermore,

the application of an IGA formulation to laminated structures can be seen in references [56–59] where interlaminar stress distribution, mid and high-range eigen-frequencies and delamination initiation and propagation phenomena can be captured accurately.

Although many applications of IGA in beam structures have been implemented successfully, the research about the synthesis of IGA and CUF is reported less frequently and should be in continuous development. Initially, Alesadi et al. [60, 61] combined CUF and IGA for free vibration and linearized buckling analyses of composite laminated plates, where 2D CUF-TE and -HLE was utilized, respectively. Subsequently, IGA was extended for the analysis of thin-walled beam structures within the framework of 1D CUF-TE [62] Equivalent Single Layer models. According to their results, higher-order B-spline functions contributed to attenuate the effect of shear locking and higher-order CUF expansions can overcome the Poisson locking phenomenon. In the present article, 1D CUF-HLE has been used in the combination of B-splines-based IGA for the geometrically linear analysis of straight beam structures. Such a combination leads to a high-fidelity computational framework with the convenience in the pre-processing stage, enabling to formulate Layer-wise models for the analysis of straight multilayered beams.

The rest of the paper is structured as follows: a brief introduction the theoretical basis of CUF formulation is introduced in Section 2; followed by a description of cross-section kinematics based on HLE in Section 3 and 1D displacement interpolation functions based on B-spline functions in Section 4. Section 5 focuses on the derivation procedure of governing equations in terms of fundamental nuclei for static, free vibration and dynamic problems. Several numerical cases are given in Section 6 to validate the accuracy and robustness of the proposed approach. Finally, the main conclusions are provided in Section 7.

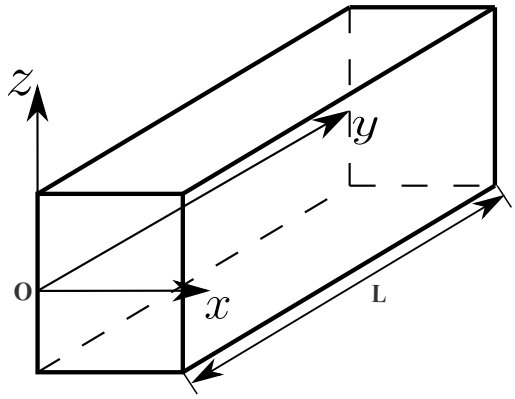

Figure 1: The global coordinate system.

2 Carrera Unified Formulation (CUF)

A beam is a typical slender structure, whose longitudinal length (L) is primary with respect to the other two orthogonal dimensions. As shown in Fig. 1, we adopt the Cartesian coordinate system as the global coordinate system for the beam structure where $x-z$ plane and $y-$axis ($0 \leq y \leq L$) are parallel and perpendicular to the cross section, respectively. The displacement vector $\mathbf{u}(x,y,z;t)$, strain vector $\boldsymbol{\epsilon}(x,y,z;t)$ and stress vector $\boldsymbol{\sigma}(x,y,z;t)$ at a specified

point of the structure can be expressed as:

$$\begin{aligned}\mathbf{u}(x,y,z;t) &= \left\{u_x\ u_y\ u_z\right\}^{\mathrm{T}}\\ \boldsymbol{\epsilon}(x,y,z;t) &= \left\{\epsilon_{yy}\ \epsilon_{xx}\ \epsilon_{zz}\ \epsilon_{xz}\ \epsilon_{yz}\ \epsilon_{xy}\right\}^{\mathrm{T}}\\ \boldsymbol{\sigma}(x,y,z;t) &= \left\{\sigma_{yy}\ \sigma_{xx}\ \sigma_{zz}\ \sigma_{xz}\ \sigma_{yz}\ \sigma_{xy}\right\}^{\mathrm{T}}\end{aligned} \tag{1}$$

where superscript "T" is the transpose operator. t is the time variable, being omitted in the remaining part for convenience.

The geometrical equations fit the linear relation and the constitutive equations obey the Hooke's law:

$$\begin{aligned}\boldsymbol{\epsilon}(x,y,z) &= \mathbf{D}\mathbf{u}(x,y,z)\\ \boldsymbol{\sigma}(x,y,z) &= \mathbf{C}\boldsymbol{\epsilon}(x,y,z)\end{aligned} \tag{2}$$

where $\mathbf{D}$ is a 6×3 differential operator matrix and $\mathbf{C}$ is the matrix of the material coefficient. One can see the references [31, 63] for their explicit forms.

Classical beam models, such as EBBM and TBM, are well-known for mechanic analysis of slender isotropic structures with the bending-dominated deformation. However, these theories are less utilized in the modeling of thin-walled and composite structures due to the poorer cross-section kinematic fields. To address this problem, CUF develops a unified beam model in which the cross-section kinematic fields can be defined by means of arbitrary functions related to x and z coordinates, as follows:

$$\mathbf{u}(x,y,z) = F_\tau(x,z)\mathbf{u}_\tau(y) \qquad \tau = 1,2,....,M \tag{3}$$

where $\mathbf{u}_\tau(y)$ is a 1D generalized displacement vector along the axis of the beam. $F_\tau(x,z)$ is the arbitrary cross-section expansion, which determines the type of the beam model. The repeated index τ stands for summation and M for the number of expansion terms.

3 Hierarchical Legendre expansions (HLE)

Hierarchical Legendre polynomials were initially exploited by Szabó et al. [64] for the construction of p-version FEM. Inspired from this work, Carrera et al. [35] made use of hierarchical Legendre polynomials as $F_\tau(x,z)$, leading to the so-called CUF-Hierarchical Legendre Expansions (HLE) beam model. In CUF-HLE, the polynomials are defined on the local natural coordinate system and mapped into the global coordinate system through the isoparametric transformation, enabling Layer-wise kinematics in a natural way. The formulation of 2D Legendre polynomials can be divided into three groups: vertex, side and internal functions. To be specific, vertex functions are introduced to create

the first-order expansions, defined as bilinear Lagrange polynomials:

$$F_\tau = \frac{1}{4}(1 + rr_\tau)(1 + ss_\tau) \qquad \tau = 1, 2, 3, 4 \tag{4}$$

where r_τ and s_τ are the coordinates of four vertexes over the quadrilateral region in the natural coordinate system. r and s vary over the interval $[-1, +1]$.

Side functions correspond to jth-order ($j \geq 2$) expansions, characterized by the significant deformation of one side and the vanishing deformation on the other three sides. Their expressions are given as follows:

$$\begin{aligned}
F_\tau(r, s) &= \tfrac{1}{2}(1 - s)\phi_j(r) \qquad \tau = 5, 9, 13, 18, \cdots \\
F_\tau(r, s) &= \tfrac{1}{2}(1 + r)\phi_j(s) \qquad \tau = 6, 10, 14, 19, \cdots \\
F_\tau(r, s) &= \tfrac{1}{2}(1 + s)\phi_j(s) \qquad \tau = 7, 11, 15, 20, \cdots \\
F_\tau(r, s) &= \tfrac{1}{2}(1 - s)\phi_j(s) \qquad \tau = 8, 12, 16, 21, \cdots
\end{aligned} \tag{5}$$

where $\phi_j(r)$ indicates 1D Legendre internal functions, see the reference [65] for further information.

As for $j \geq 4$, a set of internal functions are necessary to be added to the higher-order cross-section kinematics. The dominant deformation appears internally and vanishes on the edges. Usually, there are $j - 3$ internal functions for the jth-order expansions. Their expressions can be written in a compact manner:

$$F_\tau(r, s) = \phi_j(r)\phi_k(s) \qquad j, k \geq 2; \qquad \tau = 17, 22, 23, 28, 29, 30, \cdots \tag{6}$$

The formulations above indicate that the complete higher-order kinematics ($j \geq 4$) contain all the lower-order kinematics, i.e., vertex, side and internal functions, being capable of describing all the reasonable deformation. Due to the use of Legendre-based interpolating functions to generate the structural theory, the degrees of freedom of the model are pure displacements and higher-order modes.

4 B-spline functions

The novelty of this paper is the use of B-spline functions to approximate $\mathbf{u}_\tau(y)$. Firstly, the basic concept of B-spline functions is briefly presented, then the resulting element in the context of IGA is compared with the classical FEM element in terms of the shape function. These functions are defined recursively with the piece-wise constant representation at the starting order $p = 0$, as follows:

$$N_i^0(\xi) = \begin{cases} 1 & if\ \xi_i \leq \xi \leq \xi_{i+1} \\ 0 & otherwise \end{cases} \tag{7}$$

where ξ_i stands for the $i-$th knot.

For $p = 1, 2, 3, ...$, one obtains:

$$N_i^p(\xi) = \frac{\xi - \xi_i}{\xi_{i+p} - \xi_i} N_i^{p-1}(\xi) + \frac{\xi_{i+p+1} - \xi}{\xi_{i+p+1} - \xi_{i+1}} N_{i+1}^{p-1}(\xi) \tag{8}$$

where both N_i^0 and N_i^p are B-spline functions and p corresponds to the order.

Usually, the knot vector includes a sequence of non-decreasing coordinates in the parametric space, written as:

$$\Xi = \left\{\xi_1, \xi_2, \cdots, \xi_{n+p+1}\right\} \tag{9}$$

where n is the number of functions.

The knot vector may be uniformly or non-uniformly distributed in the parametric space, being called uniform or non-uniform B-splines, respectively. Different from the Lagrange interpolation functions, more than one knot can share the same value. This feature will play a role in the continuity $(C^1, C^2, \cdots, C^\infty)$ of the B-spline functions. For the given order p, if the first and last knots appear $p + 1$ times, the knot vector is named as the open one, i.e., endpoints interpolation. However, if the multiplicity of the internal knot is m, the knot vector has C^{p-m} continuous derivatives at that location.

Accordingly, the simple straight line can be constructed by the B-spline functions precisely, as follows:

$$y = \sum_{i=1}^{n} N_i^p(\xi)\, y_i \tag{10}$$

where y_i is the coordinate of the control point, which may fall off the curve.

Through the defintion above, $\mathbf{u}_\tau(y)$ in Eq.(3) can be approximated by the weighted linear combination of $N_i^p(\xi)$. By substitution of this approximation into Eq.(3), one can obtain:

$$\mathbf{u}(x, y, z) = F_\tau(x, z) N_i^p(\xi)\, \mathbf{q}_{\tau i} \qquad \tau = 1, 2, ..., M \qquad i = 1, 2, ..., n \tag{11}$$

where weighted coefficient $\mathbf{q}_{\tau i}$ is the generalized nodal displacement vector, the subscript τ implies the summation.

Based on the displacement pattern above, corresponding B-spline elements can be formulated, similar to the procedure in the FEM. In order to improve the analytical precision, the refinement should be subtly performed on the original coarse meshes, which can be grouped into three types: $h-$, $p-$ and $k-$types. Only $h-$type will be adopted in the paper and its mechanism lies on the knot insertion in the knot vector without changing the order of the function and the geometrical shape. For the other two types, interesting readers can refer to Hughes et al. [47].

Fig. 2 compares the shape functions of B-spline elements in IGA and Lagrange polynomial elements in FEM ($p = 2$). Corresponding models are defined by the symbolization: $\alpha B\beta$ and $\alpha L\beta$, in which α and β refer to the number of the elements and control points per single element. B and L stand for B-spline and Lagrange polynomial functions, respectively. For example, 2B3 means there are two quadratic B-spline elements in the $y-$axis direction. Each element has three control points.

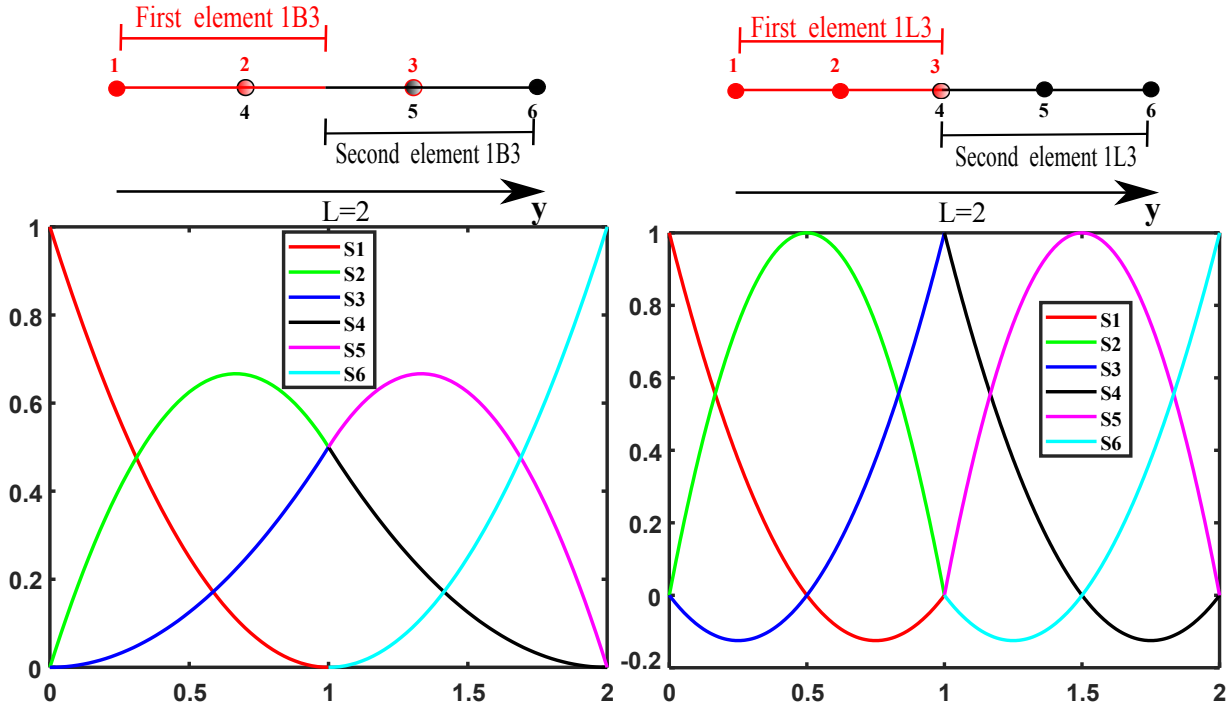

(a) $2B3$ (b) $2L3$

Figure 2: Comparison of the shape functions.

From the figure, some useful information can be obtained. In IGA, less control points are needed. Besides, control points may not fall into the range of the element to which they belong, giving rise to the C^1 continuity condition between the elements; while in FEM, the interpolation property is satisfied everywhere, thus leading to the C^0 continuity of the inter elements.

5 Governing equations

The governing equations of a generic beam structure in a Cartesian reference frame can be derived via the variational principle of virtual work. For static, free vibration and dynamic cases, they hold:

$$\begin{aligned} \delta L_{\text{int}} &= \delta L_{\text{ext}} \\ \delta L_{\text{int}} &= -\delta L_{\text{ine}} \\ \delta L_{\text{int}} &= \delta L_{\text{ext}} - \delta L_{\text{ine}} \end{aligned} \tag{12}$$

where δ denotes the symbol of the virtual variation. L_{int} is the strain energy, L_{ine} indicates the inertial work, L_{ext} represents the work done by the external force.

5.1 Stiffness matrix

The virtual variation of strain energy can be written as:

$$\delta L_{\text{int}} = \int_V \delta \boldsymbol{\epsilon}^{\mathrm{T}} \boldsymbol{\sigma} \mathrm{d}V \tag{13}$$

where V is the volume.

Consider the geometrical relations and constitutive law under the assumption of small displacements, rotations and deformations, as follows:

$$\boldsymbol{\epsilon} = \mathbf{D}\mathbf{u}, \quad \boldsymbol{\sigma} = \mathbf{C}\boldsymbol{\epsilon} \tag{14}$$

where $\mathbf{D}$ is 6×3 differential operator matrices. $\mathbf{C}$ is 6×6 stiffness matrices of the material. The explicit formulations of $\mathbf{D}$ and $\mathbf{C}$ have already been reported in the literature [66].

By substituting geometrical and constitutive equations in Eq. (2) and the displacement assumption in Eq. (3) into Eq. (13), one has:

$$\delta L_{\text{int}} = (\delta \mathbf{q}_{sj})^{\mathrm{T}} \int_V R_j^p F_s \mathbf{D}^{\mathrm{T}} \mathbf{C} \mathbf{D} F_\tau R_i^p \mathrm{d}V \, \delta \mathbf{q}_{\tau i} = (\delta \mathbf{q}_{sj})^{\mathrm{T}} \mathbf{K}_e^{\tau sij} \mathbf{q}_{\tau i} \tag{15}$$

where $\mathbf{K}_e^{\tau sij}$ is the fundamental nucleus of the element stiffness matrix, which is composed of 3×3 matrices.

$$\mathbf{K}_e^{\tau sij} = \begin{bmatrix} K_{e(11)}^{\tau sij} & K_{e(12)}^{\tau sij} & K_{e(13)}^{\tau sij} \\ K_{e(21)}^{\tau sij} & K_{e(22)}^{\tau sij} & K_{e(23)}^{\tau sij} \\ K_{e(31)}^{\tau sij} & K_{e(32)}^{\tau sij} & K_{e(33)}^{\tau sij} \end{bmatrix} \tag{16}$$

In the case of laminated structures with orthotropic material, their explicit formulations are given in APPENDIX A.

The components of the fundamental nucleus in the element stiffness matrix remain unaltered when different types of the beam model and shape functions are chosen. This form of invariance implies that the global stiffness matrix of arbitrary types of the beam model can be conveniently implemented by appropriately setting the loop statements featured by the indexes τ, s, i and j in the code.

Fig. 3 outlines the differences in the assembly process of global stiffness matrices between IGA 1D CUF-HLE and FEM 1D CUF-HLE. In detail, the same cross-section kinematics (1×1HL2) and number of elements are considered for both models, in which 1×1 represents the number of solid cross-section subdomains in the x and z directions and HL2 means that the order of Legendre polynomials is 2. Alternatively, for the thin-walled structure, we use the notation θHL2, in which θ stands for the total number of cross-section subdomains.

From this figure, it can be seen that the difference of the assembly process for two models resides in the last step, i.e., from the element stiffness matrix to global stiffness matrix. Unlike FEM 1D CUF-HLE, the multiplicities of knot values lead to non-interpolation behavior of node variables in IGA 1D CUF-HLE as there are mode shared nodes between elements. Such features decrease the size of the global stiffness matrix, and computation costs compared with

FEM 1D CUF-HLE as well.

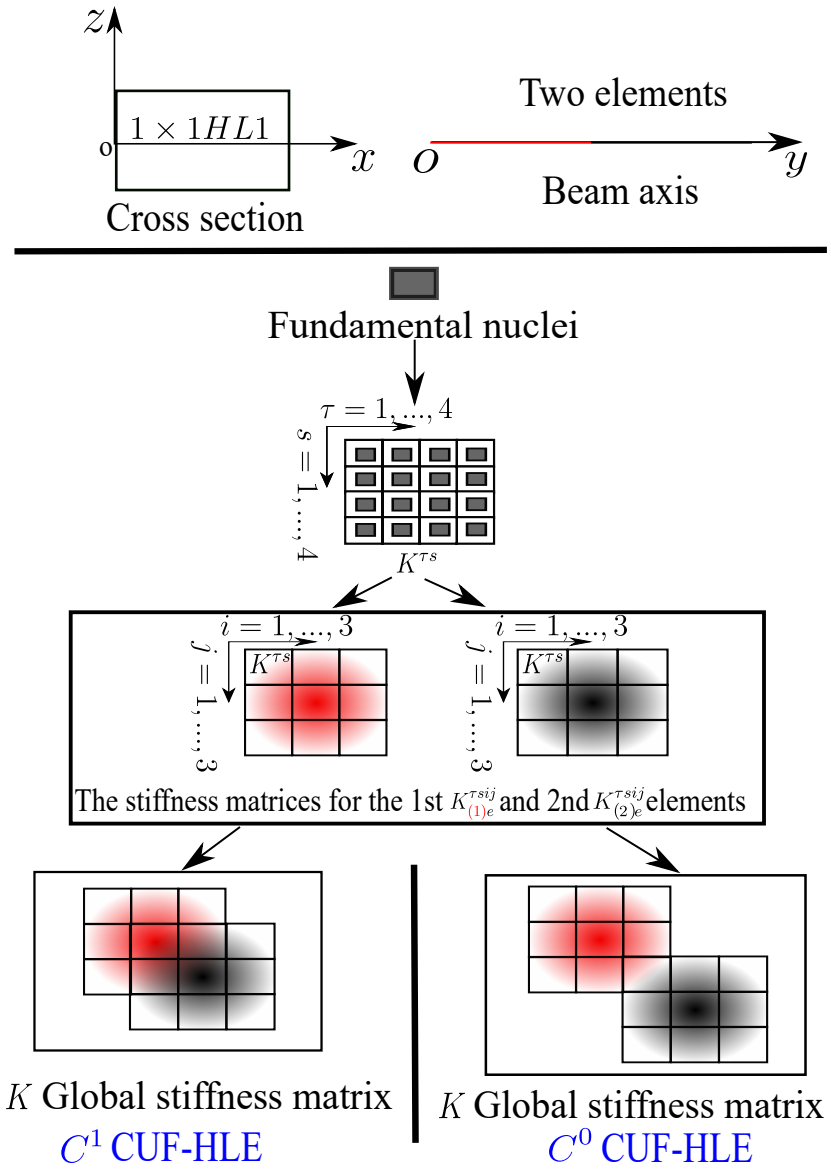

Figure 3: The assembly process of global stiffness matrices for two models.

5.2 Loading vector

In the case of the concentrated load $\mathbf{F} = \left\{F_x, F_y, F_z\right\}$ acting at the point (x_c, y_c, z_c), the work done by the external force can be expressed as:

$$\delta L_{\text{ext}} = \delta \mathbf{u}^{\text{T}} \mathbf{F} \tag{17}$$

Other types of loading condition, such as line and surface loads, can be treated in a similar way. By substitution of Eq. (11) into Eq. (17), it reads:

$$\delta L_{\text{ext}} = \delta \mathbf{q}_{\tau i}^{\text{T}} F_\tau R_i^p \mathbf{F} = \delta \mathbf{q}_{\tau i}^{\text{T}} \tag{18}$$

where F_τ and R_i^p are evaluated at the corresponding position (x_c, z_c) and (y_c), $\mathbf{P}_e^{\tau i}$ is the element nodal load vector.

5.3 Mass matrix

The virtual variation of inertial work can be expressed as:

$$\delta L_{\text{ine}} = \int_V \delta \mathbf{u}_\tau^{\mathrm{T}} \rho \ddot{\mathbf{u}}_s \mathrm{d}V \tag{19}$$

where superimposed dots denote the second derivative with respect to time, substituting Eq. (11) into Eq. (19), it holds:

$$\delta L_{\text{ine}} = \int_V \delta \mathbf{q}_{\tau i}^{\mathrm{T}} (J_{ij} \triangleleft \rho F_\tau F_s \triangleright) \mathbf{I}) \ddot{\mathbf{q}}_{sj} \mathrm{d}V = \delta \mathbf{q}_{\tau i}^{\mathrm{T}} \mathbf{M}_e^{\tau s i j} \ddot{\mathbf{q}}_{sj} \tag{20}$$

where symbols J_{ij} and $\triangleleft \cdot \triangleright$ can be found in APPENDIX A, $\mathbf{I}$ is a 3×3 identity matrix. $\mathbf{M}_e^{\tau s i j}$ is the element mass matrix.

It should be pointed out that $\mathbf{P}_e^{\tau i}$ and $\mathbf{M}_e^{\tau s i j}$ can be analogously assembled into the global nodal load vector and mass matrix, as already demonstrated in Fig. 3.

5.4 Algebraic expressions of governing equations

The static analysis inquires into the equilibrium between internal and external forces. Considering Eq. (15) and Eq. (12), the final algebraic system of governing equations as proposed in Eq. (12) is obtained

$$\mathbf{K}\mathbf{q} = \mathbf{P} \tag{21}$$

The free vibration analysis investigates the equilibrium between elastic and inertial forces. As already discussed in Section 5.1 and 5.3, the principle of virtual displacements in this problem is formulated as

$$\mathbf{K}\mathbf{q} + \mathbf{M}\ddot{\mathbf{q}} = 0 \tag{22}$$

When harmonic motion is taken into account, the solution of $\mathbf{q}$ can be resolved into the product of the amplitude function of the motion $\mathbf{Q}$ and the natural frequency (ω)-related function $e^{i\omega t}$. Thus, Eq. (22) can be simplified into a classical eigenvalue problem:

$$(\mathbf{K} - \omega^2 \mathbf{M})\mathbf{Q} = 0 \tag{23}$$

In the more general case, both internal, external and inertial energy contributions are accounted for in the dynamic problem. Therefore, the algebraic system of governing equations become

$$\mathbf{K}\mathbf{q} + \mathbf{M}\ddot{\mathbf{q}} = \mathbf{P} \tag{24}$$

Eq. (24) represents a system of linear differential equations of second order with constant coefficient and can

be usually solved by two kinds of time integration schemes: explicit and implicit approaches. In this article, the improved Newmark β-based implicit approach is employed for the temporal discretization of the equations due to its unconditionally stable. Besides, this method is proved to be superior for the measure of the numerical dispersion and dissipation [67]. This effective scheme is listed as follows:

$$\begin{aligned}
&\mathbf{M}\ddot{\mathbf{q}}_{t+\Delta t} + (1+\gamma)\mathbf{K}\mathbf{q}_{t+\Delta t} - \gamma\mathbf{K}\mathbf{q}_{t+\Delta t} = \mathbf{P}_{t+\Delta t} \\
&\mathbf{q}_{t+\Delta t} = \left(\mathbf{K} + \tfrac{1}{\alpha\Delta t^2}\mathbf{M}\right)^{-1}\left(\mathbf{P}_{t+\Delta t} + \mathbf{M}\left(\tfrac{1}{\alpha\Delta t^2}\mathbf{q}_t + \tfrac{1}{\alpha\Delta t}\dot{\mathbf{q}}_t + (\tfrac{1}{2\alpha} - 1)\ddot{\mathbf{q}}_t\right)\right) \\
&\ddot{\mathbf{q}}_{t+\Delta t} = \tfrac{1}{\alpha\Delta t^2}\left(\mathbf{q}_{t+\Delta t} - \mathbf{q}_t\right) - \tfrac{1}{\alpha\Delta t}\dot{\mathbf{q}} - (\tfrac{1}{2\alpha} - 1)\ddot{\mathbf{q}}_t \\
&\dot{\mathbf{q}}_{t+\Delta t} = \dot{\mathbf{q}} + (1-\beta)\,\Delta t\ddot{\mathbf{q}}_t + \beta\Delta t\ddot{\mathbf{q}}_{t+\Delta t}
\end{aligned} \tag{25}$$

where Δt is the time increment. $\dot{\mathbf{q}}$ and $\ddot{\mathbf{q}}$ represent the vector of nodal velocities and accelerations. $\alpha = 0.25(1-\gamma)^2$, $\beta = 0.5 - \gamma$ and $\gamma \in \left[-\frac{1}{3}, 0\right]$.

With the reduction of γ in the admission range, the numerical dispersion can be eliminated effectively. More details about its efficiency are discussed in the following numerical examples.

6 Numerical results

In this section, six numerical cases are given to demonstrate the accuracy of the proposed approach for static, free vibration and dynamic problems. The calculation results are compared with FEM 1D CUF-HLE and 3D FEM solutions as well as those from the literatures. Without special notification, the order of B-spline functions is 2 and the full integration is used in all cases.

6.1 Bending analysis

A single-bay composite box beam is considered as the preliminary assessment, as shown in Fig. 4. Its dimensions are: width $b = 24.2$ mm, height $h = 13.6$ mm, Length $L = 242$ mm, flange and web with the equal thickness $t = 0.762$ mm. Different stacking sequences are chosen: $[0°/90°]$ for the flange and $[-45°/45°]$ for the web, being $[0°]$ and $[-45°]$ laminations on the outside. Each lamina is composed of an orthotropic material with the properties parallel (L) and perpendicular (T) to the fibre: Young moduli $E_L = 69.0$ GPa and $E_T = E_Z = 10.0$ GPa; Poisson ratio $\nu_{LT} = \nu_{LZ} = \nu_{TZ} = 0.25$; Shear moduli $G_{LT} = G_{LZ} = G_{TZ} = 6.0$ GPa; Material density $\rho = 2700$ kg/m^3. Two point forces ($2 \times P = 2 \times 50$ N) are applied at the upper corners of the cross-section $[:, L, :]$. The cross-section kinematics are made of one sub-domain per layer (8HL4).

Table 1 compares the transverse displacement (u_z) and axial stress (σ_{yy}) and shear stress (σ_{yz}) values at different evaluation points obtained by FEM 1D CUF-HLE and IGA 1D CUF-HLE. Three- and four-node longitudinal discretizations are employed for FEM 1D CUF-HLE and the three-node longitudinal discretization for IGA 1D CUF-HLE. Taking 12L4 as reference, it is possible to see that 16L3 produces more accurate results than 16B3. This interesting

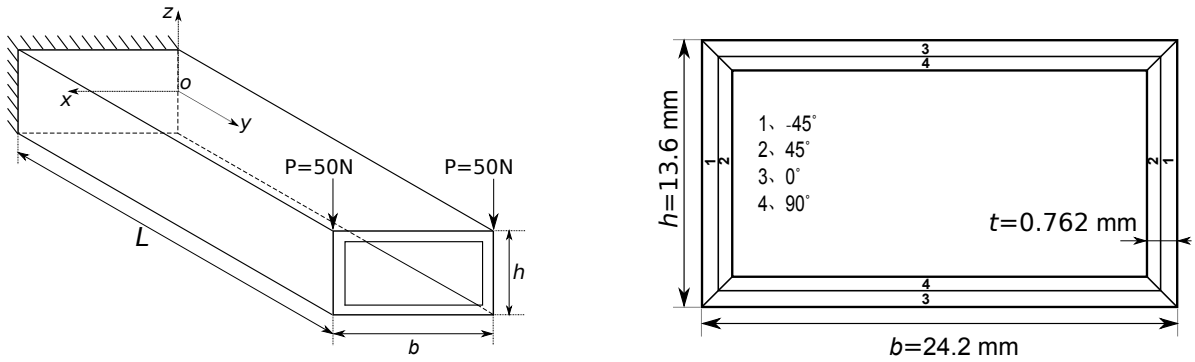

Figure 4: Geometrical shape, loading condition and layup of the composite box beam.

phenomenon means in the case of the same number of elements for both models, IGA 1D CUF-HLE is superior to FEM 1D CUF-HLE. However, when DOFs of both models are almost equal each other, FEM 1D CUF-HLE shows faster convergence than IGA 1D CUF-HLE (see 16L3 and 32B3).

Table 1: Displacement and stress results at the evaluation points (8HL4)

Model	DOFs	$u_z \times 10^3$ [m]	$\sigma_{yy} \times 10^{-6}$ [Pa]	$\sigma_{yy} \times 10^{-6}$ [Pa]	$\sigma_{yz} \times 10^{-6}$ [Pa]
		$[0, L/2, +h/2]$	$[0, L/2, +h/2]$	$[0, 0, +h/2]$	$[b, L/2, 0]$
FEM 1D CUF-HLE					
9L3	4560	-7.098	83.706	173.341	-3.837
16L3	7920	-7.109	84.465	178.488	-4.962
8L4	6000	-7.111	83.713	181.887	-4.488
12L4	8880	-7.113	83.727	181.887	-4.487
IGA 1D CUF-HLE					
16B3	4320	-7.106	83.719	175.723	-5.014
32B3	8160	-7.114	83.729	183.005	-4.618

Fig. 5 plots the variations of u_z and σ_{yy} along the line $(b/2, :, h/2-t/4)$ and σ_{yz} along the line $(b-t/4, :, 0)$ computed by different models. It can be found that values of u_z, σ_{yy} are less sensitive to longitudinal meshes compared to those of σ_{yz}. To be specific, shear stresses provided by quadratic FEM models exhibit prominent oscillatory behaviors, followed by cubic FEM models oscillating only around both ends. Quadratic IGA models show less oscillations which are concentrated towards the ends, yielding more precise solutions over the length of the beam. Moreover, due to the use of C^1 continuous B-splines, the continuity of the stresses along the axis is respected. Indeed, the inability of standard FEM models to compute the right shear stresses is the cause of the well-known shear locking issue.

6.2 Free vibration analysis

To test the validity of the proposed model on the free vibration problem, we consider a clamped-clamped sandwich beam consisting of two faces and a soft core. Two faces have the same geometric parameters and material properties. The geometric parameters of the beam are: width $b = 25.4$ mm, height $h = 25.4$ mm, length $L = 127$ mm, the thicknesses of the top face $h_t = 2.54$ mm and the bottom face $h_b = 2.54$ mm. Both the face (f) and core (c) are assumed

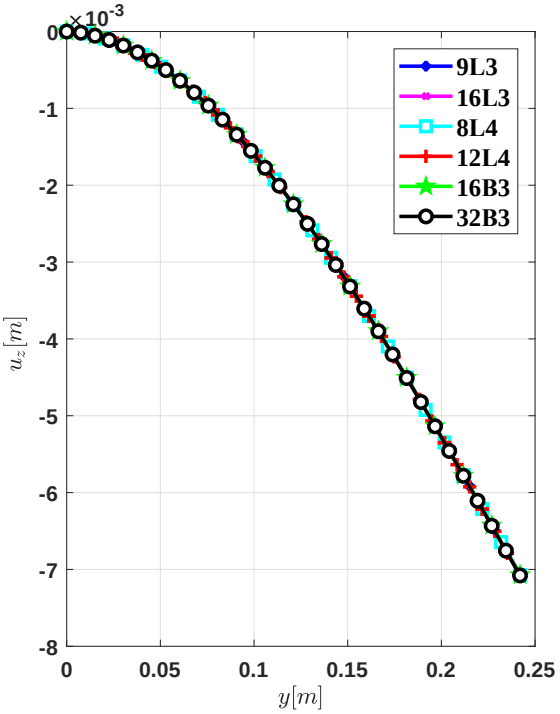

(a) u_z, $(b/2, :, h/2 - t/4)$

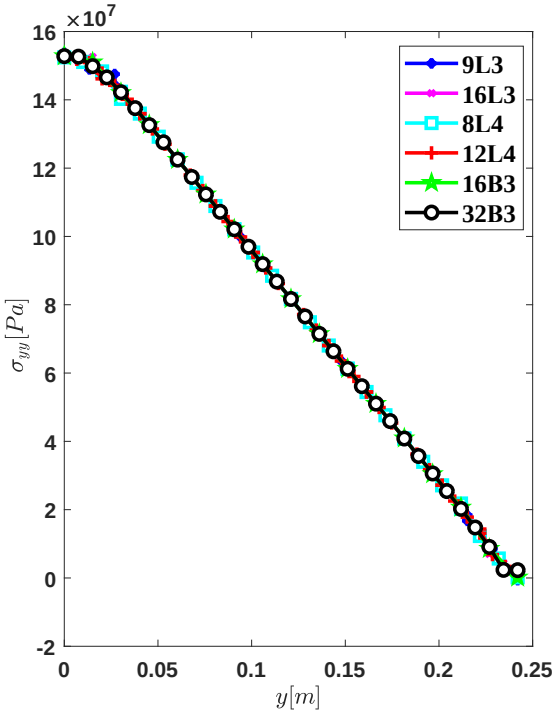

(b) σ_{yy}, $(b/2, :, h/2 - t/4)$

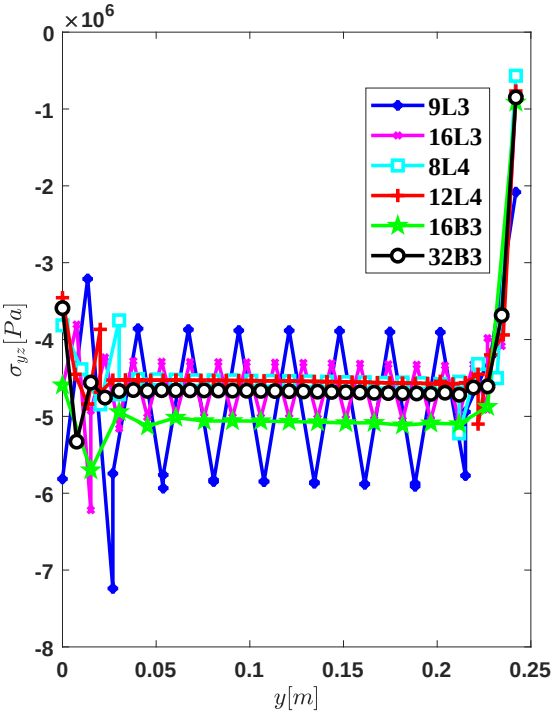

(c) σ_{yz}, $(b - t/4, :, 0)$

Figure 5: Distributions of transverse displacement u_z and stress components σ_{yy} and σ_{yz} along the longitudinal direction.

to be isotropic with the following mechanical properties: Young moduli E_f = 68.9 GPa and E_c = 179.014 MPa; shear moduli G_f = 26.5 GPa and G_c = 68.9 Mpa; material density ρ_f = 2687.3 kg/m^3 and ρ_c = 119.69 kg/m^3.

Table 2: The non-dimensional natural frequencies ω^* from 1 to 5 with 32B3

Mode	DOFs	mode 1[d]	mode 2[e]	mode 3[f]	mode 4[g]	mode 5[h]
ABAQUS[a]	6894	2.038	4.408	6.695	7.365	7.784
ABAQUS[b]	10263	2.037	4.406	6.684	7.361	7.779
ABAQUS[c]	178119	2.031	4.391	6.658	7.329	7.769
IGA 1D CUF-1 × 3HL4	4182	2.031	4.391	6.742	7.330	7.776
IGA 1D CUF-1 × 3HL5	5814	2.031	4.391	6.678	7.329	7.772
IGA 1D CUF-2 × 3HL4	7038	2.031	4.391	6.686	7.327	7.772
IGA 1D CUF-2 × 3HL5	9996	2.031	4.389	6.669	7.324	7.769

[a]: The number of elements is 3 × 26 × 5
[b]: The number of elements is 4 × 26 × 6
[c]: The number of elements is 20 × 26 × 26
[d]: First flexural mode on plane yz; [e]: Second flexural mode on plane yz; [f]: First torsional mode
[g]: Third flexural mode on plane yz; [h]: First flexural (plane xy) / tosional mode

Different from the last case, this case mainly investigates the influence of HLE variable kinematics on the first ten non-dimensional natural frequencies ω^* when keeping the type of longitudinal mesh as 32B3 constantly. All the non-dimensional results can be achieved through the formulation: $\omega^* = (\omega L^2/b)\sqrt{\rho_f/G_f}$, which are listed in Table 2 and 3. ABAQUS models can be classified into three types according to different numbers of elements discretized along two orthogonal directions lying on the cross-section. Almost all the results obtained with three ABAQUS models show good convergence with the exception of mode switching between mode 6 and 7 by ABAQUS^a and ABAQUS^b. IGA 1D CUF-HLE models are developed by choosing various expansion discretizations and orders. Similar to the phenomena observing in ABAQUS models, mode switching problems can be solved by increasing the kinematics over the cross-section while maintaining lower computational costs compared with ABAQUS models. Besides, IGA 1D CUF-1×3HL5 performs better than IGA 1D CUF-2 × 3HL4 in the prediction of torsional and core modes, which demonstrates that such models with higher-order expansions are more efficient than those with more expansional sub-domains in capturing non-classical modes.

Table 3: The non-dimensional natural frequencies ω^* from 6 to 10 with 32B3

Mode	DOFs	mode 6[d]	mode 7[e]	mode 8[f]	mode 9[g]	mode 10[h]
ABAQUS[a]	6894	**10.659**	10.627	10.732	10.803	11.025
ABAQUS[b]	10263	**10.623**	10.614	10.721	10.787	11.019
ABAQUS[c]	178119	10.539	10.592	10.698	10.754	10.960
IGA 1D CUF-1 × 3HL4	4182	**10.861**	10.649	10.748	10.828	10.958
IGA 1D CUF-1 × 3HL5	5814	10.612	10.630	10.732	10.809	10.957
IGA 1D CUF-2 × 3HL4	7038	10.637	10.644	10.738	10.791	10.953
IGA 1D CUF-2 × 3HL5	9996	10.581	10.624	10.726	10.785	10.948

[a]: The number of elements is 3 × 26 × 5
[b]: The number of elements is 4 × 26 × 6
[c]: The number of elements is 20 × 26 × 26
[d]: Second torsional mode; [e]: First core mode; [f]: Second core mode; [g]: First shear mode on plane xz
[h]: Fourth flexural mode on plane yz; [i]: Not provided

The contour plots of torsional, shear and core modes provided by 2 × 3HL5 and ABAQUS^b are shown in Fig. 6.

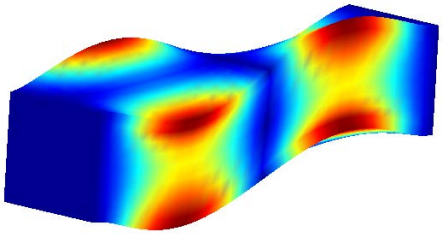

(a1) Second torsional mode, 2×3 HL5

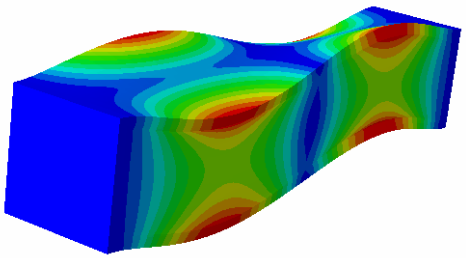

(b1) Second torsional mode, ABAQUS^b

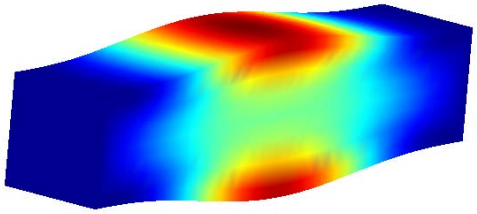

(a2) First core mode, 2×3 HL5

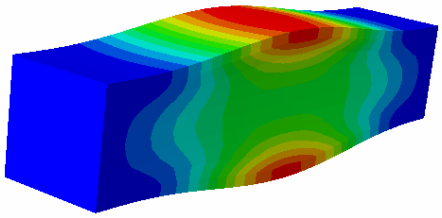

(b2) First core mode, ABAQUS^b

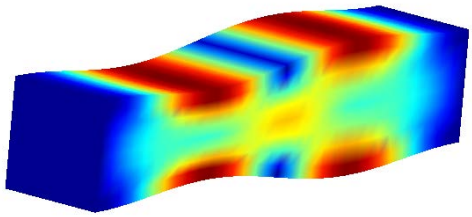

(a3) Second core mode, 2×3 HL5

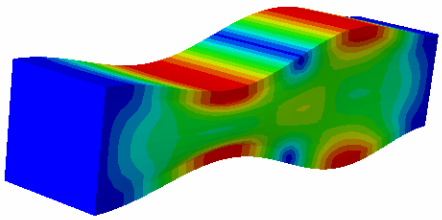

(b3) Second core mode, ABAQUS^b

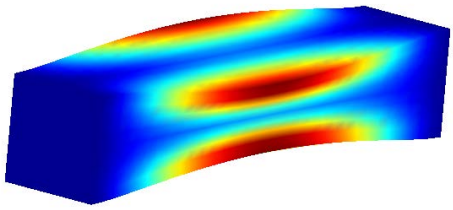

(a4) First shear mode on plane xz, 2×3 HL5

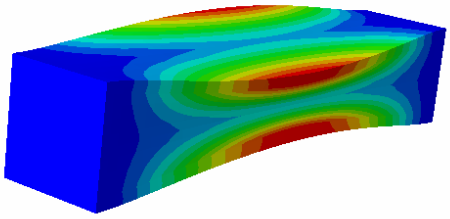

(b4) First shear mode on plane xz, ABAQUS^b

Figure 6: Comparison of non-classical modes by IGA 1D CUF-2×3HL5 and ABAQUS models.

It can be seen that results of the two methods are in high agreement where the torsional and shear modes belong to the global mode, characterized by the cross-section warping whereas core modes belong to the local mode, characterized by the cross-section distortion.

6.3 Dynamic analysis

This section extends the application of the proposed method to solve elastodynamic problems of beam structures. Special attention is given to the impulse and moving loads.

6.3.1 Metallic beam subjected to a lateral impulse load

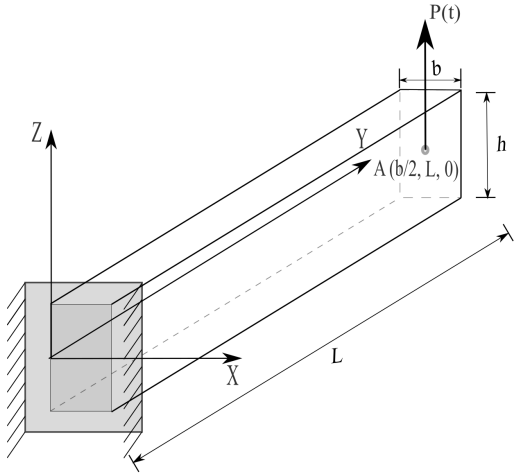

Figure 7: The computational model for the metallic beam.

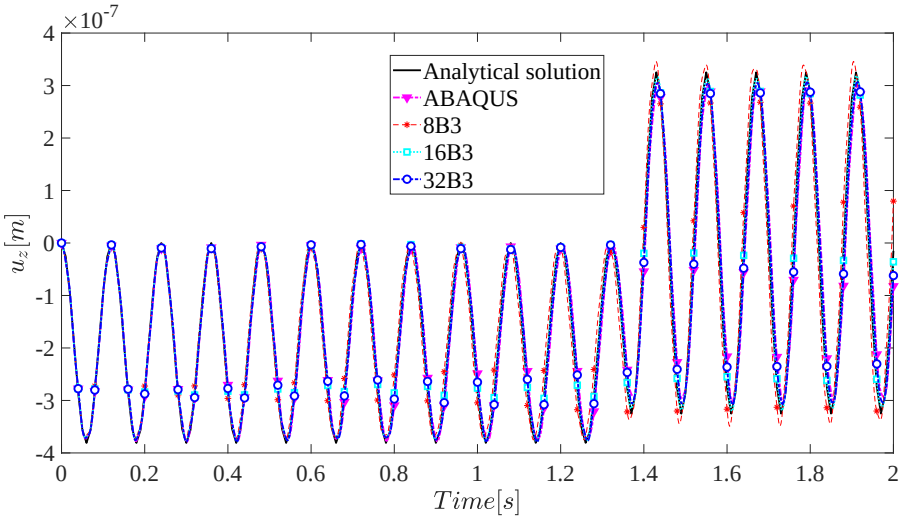

Figure 8: Time history of u_z at point A for various NURBS elements.

A cantilever isotropic beam with the rectangular cross section subjected to a step load is analyzed. This step load is applied at the middle of the cross-section $[:, L, :]$ (see Fig. 7) and can be formulated using the Heaviside function: $P(t) = P_0 \times H(t - 1.36)$ with P_0 equal to 10 N. The slenderness ratio L/h, the thickness h and width b are 10, 1 m, 1

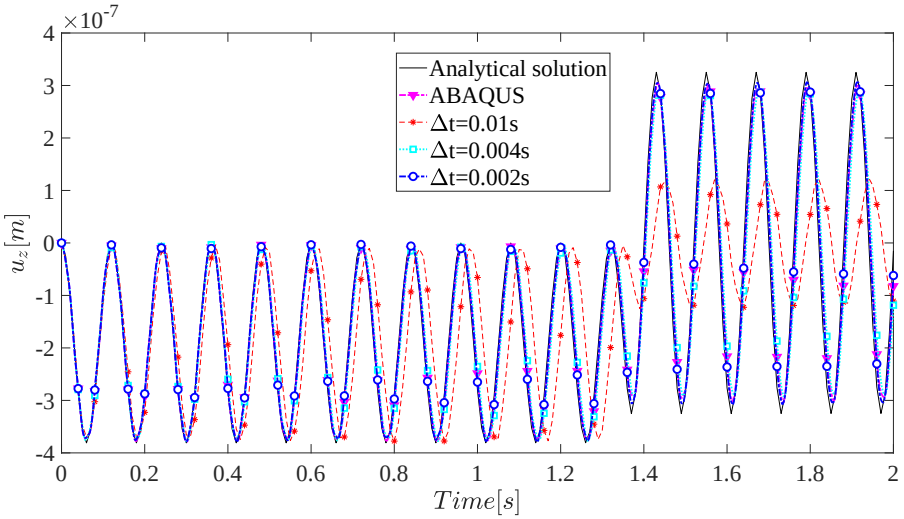

Figure 9: Time history of u_z at point A for various time steps with 32B3.

m, respectively. The material properties are as follows: Young modulus $E = 210$ GPa; Poisson ratio $\nu = 0.3$; material density $\rho = 7900$ kg/m^3.

Fig. 8 shows the influence of the number of B-spline elements, being the cross-section kinematics fixed as 1×1HL2 and the time step as 0.002 s. ABAQUS and analytical solutions are given for comparison purposes. The type, number and time step of the ABAQUS model are C3D20, $2 \times 20 \times 2$ and 0.002 s, respectively, and the analytical solution is derived based on the Euler-Bernoulli beam model:

$$u_z(t) = \left[1 - cos(\frac{2\pi}{T}t)\right] \frac{4P_0L^3}{Ebh^3} \tag{26}$$

where $T = \frac{2\pi}{1.875^2}\sqrt{\frac{12\rho L^4}{Eh^2}}$ is the structural natural vibration period.

As indicated in Fig. 8, the analytical solution and 8B3 model lead to less accurate estimations in comparison with other models, but only by a small margin. In the subsequent analysis, 32B3 model is employed to guarantee the accuracy with reference to the ABAQUS model. It should be noted that the analytical solution performs worst due to less cross-section kinematics.

Accordingly, Fig. 9 compares the displacement-time curve of point A $(b/2, L, 0)$ considering various time steps. Again, the analytical solution and the solution with a larger time step 0.01 s are not able to provide the curve closer to the ABAQUS solution. The time step 0.002 s is chosen for further investigation.

Fig. 10 and 11 plot the variation of u_z and σ_{yy} along the y-axis varying the cross-section kinematics at different times. It can be observed that, when u_z of point A is in the large amplitude condition, the cross-section kinematics have almost no impact on the values of these two variables. However, when u_z of point A is in the small amplitude condition, 1×1HL2 cannot give good approximations for both variables.

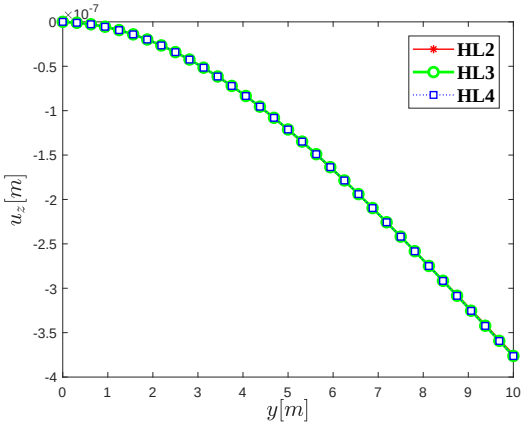

(a) u_z at $(x, y, z) = (b/2, :, -h/2)$

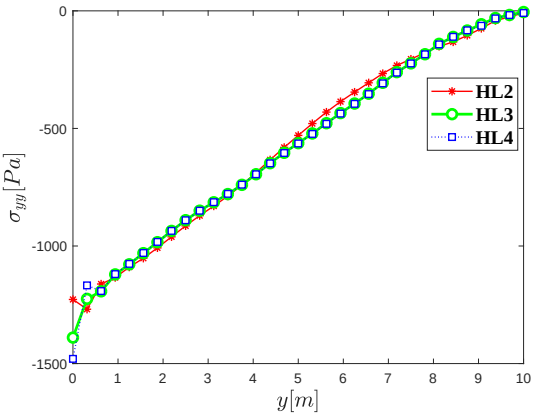

(b) σ_{yy} at $(x, y, z) = (b/2, :, -h/2)$

Figure 10: Distributions of u_z and σ_{yy} along the beam axis for different cross-section kinematics at $t = 0.18$ s with 32B3.

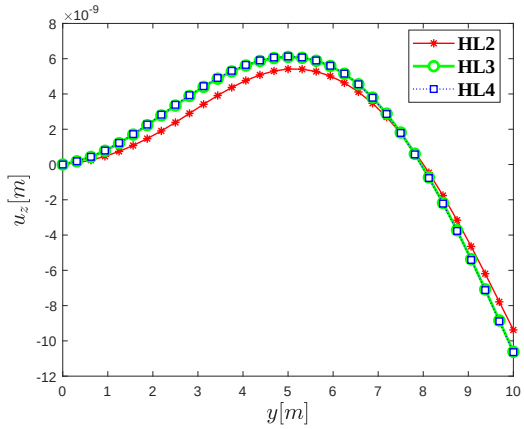

(a) u_z at $(x, y, z) = (b/2, :, -h/2)$

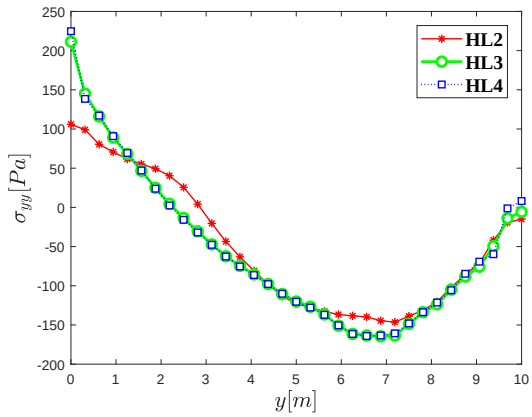

(b) σ_{yy} at $(x, y, z) = (b/2, :, -h/2)$

Figure 11: Distributions of u_z and σ_{yy} along the beam axis for different cross-section kinematics at $t = 0.24$ s with 32B3.

6.3.2 Stress wave propagation in a metallic bar

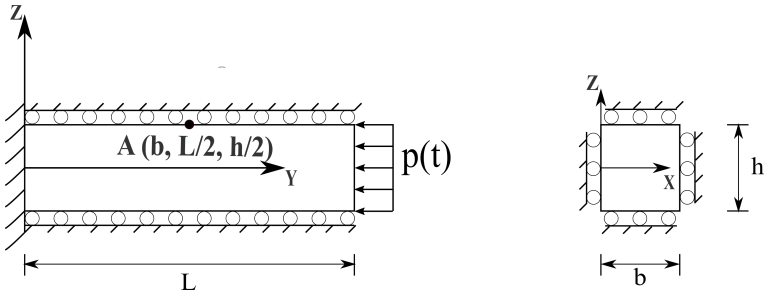

Figure 12: The geometrical shape for the clamped bar.

This case deals with a classical 1D wave propagation problem. The blast pressure is perpendicularly acted on the cross section at free end of the beam structure, which can be also represented using Heaviside function: $P(t) = P_0 \times H(t - 3.88 \times 10^{-5})$ with P_0 equal to1×10^5 Pa. The width, b and height, h are $b = h = 0.2$ m with the slenderness ratio $L/h = 5$. The material properties are considered as isotropic: Young modulus $E = 207$ GPa; Poisson ratio $\nu = 0.3$; material density $\rho = 7800$ kg/m^3. Concerning the boundary conditions, the cross-section at the left end is fully clamped and all the lateral edges are partially clamped, namely, $u_x = u_z = 0$, as shown in Fig. 12.

Fig. 13- 15 compare the distributions of u_y, σ_{yy} and v_y along the line $(x, y, z) = (b, :, h/2)$ attained with the proposed model and ABAQUS model for three typical times. In our model, the cross-section kinematics and time step are 1×1HL2 and 1.5×10^{-7} s, while in ABAQUS model, the C3D20 solid element with the number $3 \times 65 \times 3$ is employed and the time step of 1.5×10^{-7} s is determined. Both models are solved by the implicit scheme based on the improved Newmark β. The first selected time denotes the wave in the forward-propagating stage, the second selected time denotes the superposition of the incident wave and reflected wave near the clamped end and the third selected time denotes the wave in the backward-propagating stage. Inspecting these figures, u_y is only slightly influenced by the number of elements and parameter γ, which yet have deleterious effects on σ_{yy} and v_y. An insufficient number of elements will give rise to the numerical dispersion error. For instance, σ_{yy} and v_y cannot be approximated to zero near the pressure-carrying end (see Fig. 14 and Fig. 15). In the meanwhile, inappropriate γ value will result in spurious oscillations of the wave front. Specifically, model 256B3, $\gamma = -0.05$ can suppress spurious oscillations in a great manner with respect to model 256B3, $\gamma = 0$. Besides, the ABAQUS model cannot achieve the same effect due to C^0 continuity condition of the interelement even if γ is equal to -0.05.

Fig. 16 reports the axial displacement- and velocity-time relations at the point A $(b, L/2, h/2)$ for different time steps. Again the results demonstrate that the time step is not an important factor in the description of the axial displacement-time curve, but plays a certain role in the description of the axial velocity-time curve within a certain range, i.e., $\Delta t \geq 1.5 \times 10^{-7}$. Out of this range, shorter time step will not damp out the spurious oscillations and reduce numerical dispersion errors. The underlying reason is that quadratic IGA models with limited elements can simulate the lower frequency components. It is true that the wave spectrum during the propagation process not only includes lower frequency components, but also higher frequency components. By adjusting the value of parameter γ, correspond-

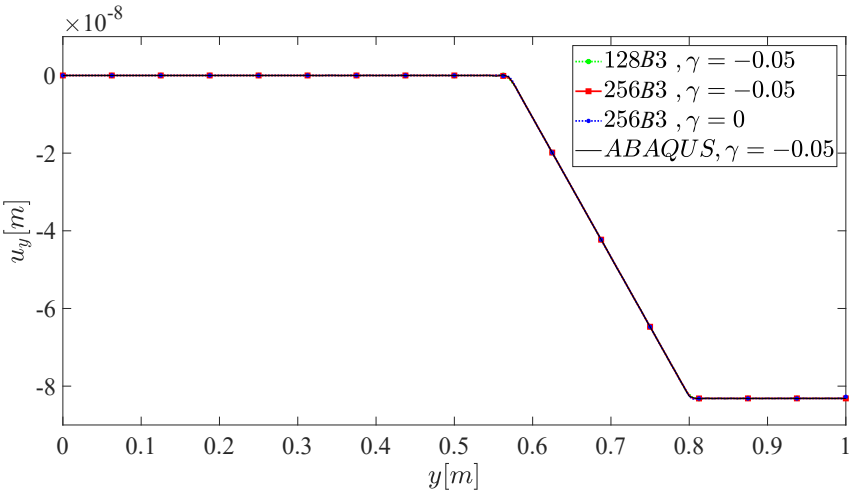

(a) $t = 7.2 \times 10^{-5}$ s

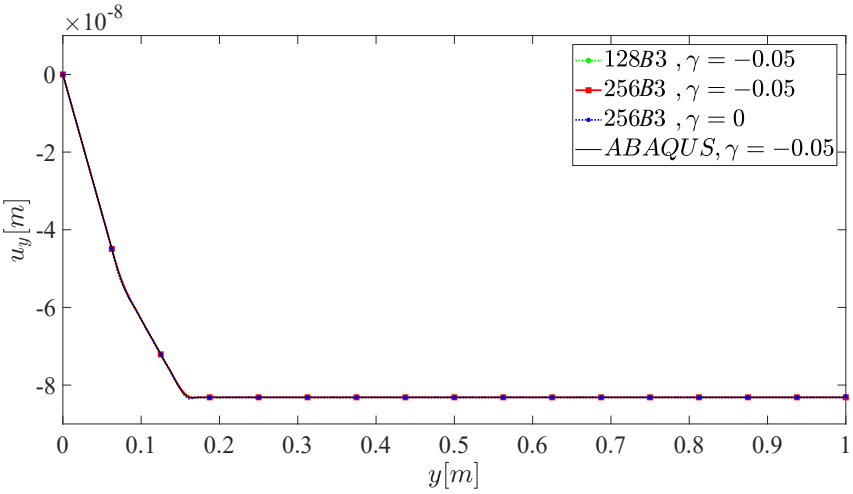

(b) $t = 1.8 \times 10^{-4}$ s

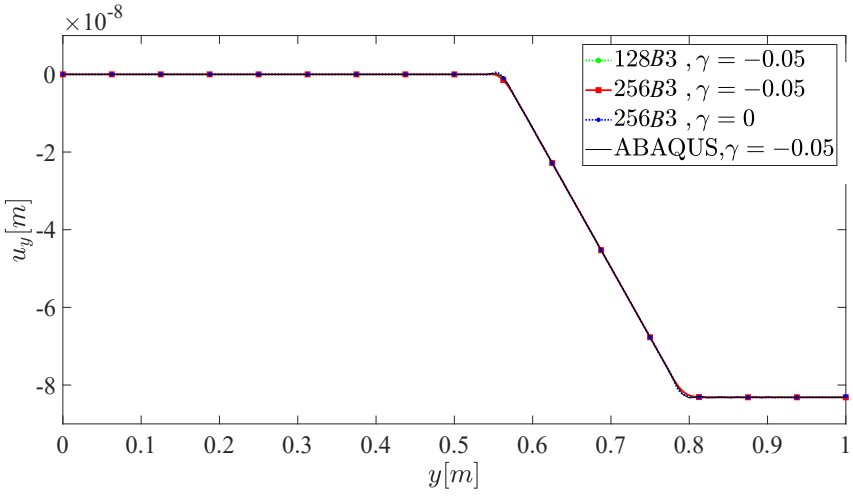

(c) $t = 3.0 \times 10^{-4}$ s

Figure 13: Through-the-length variation of u_y at $(x, y, z) = (b, :, h/2)$.

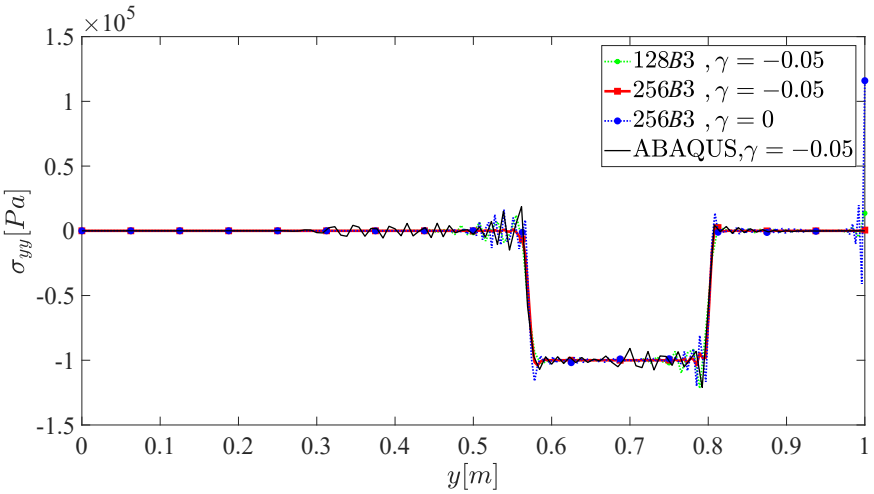

(a) $t = 7.2 \times 10^{-5}$ s

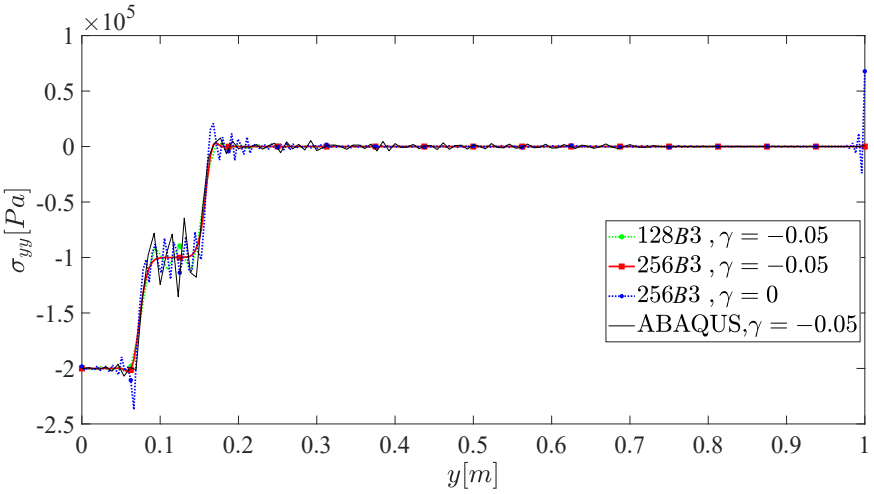

(b) $t = 1.8 \times 10^{-4}$ s

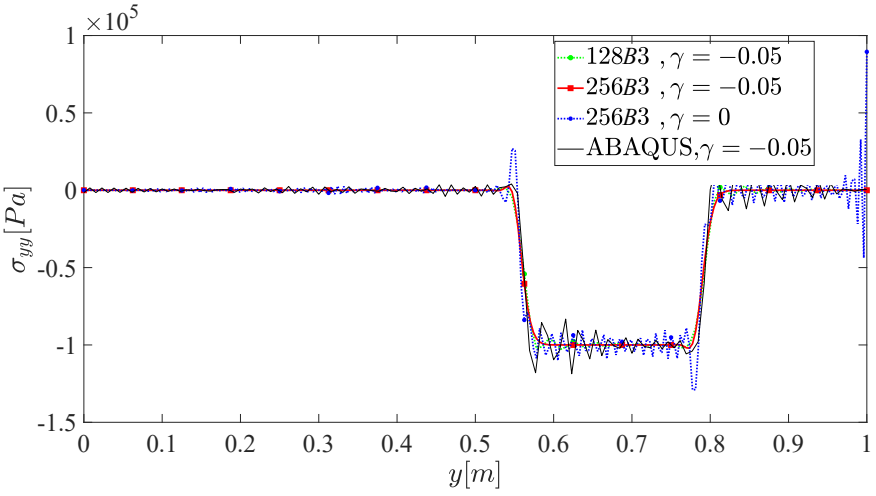

(c) $t = 3.0 \times 10^{-4}$ s

Figure 14: Through-the-length variation of σ_{yy} at $(x, y, z) = (b, :, h/2)$.

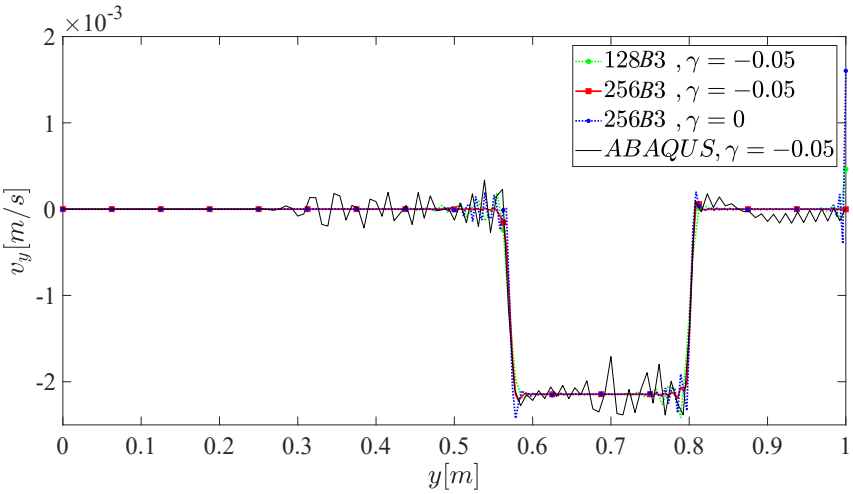

(a) $t = 7.2 \times 10^{-5}$ s

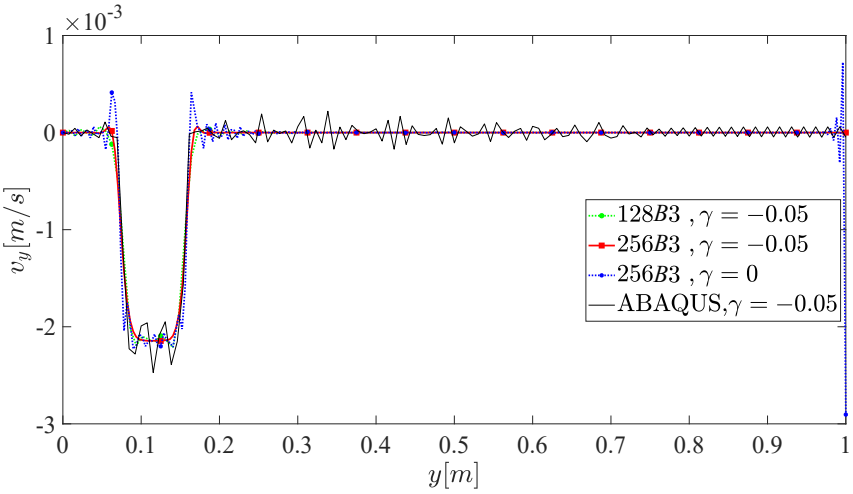

(b) $t = 1.8 \times 10^{-4}$ s

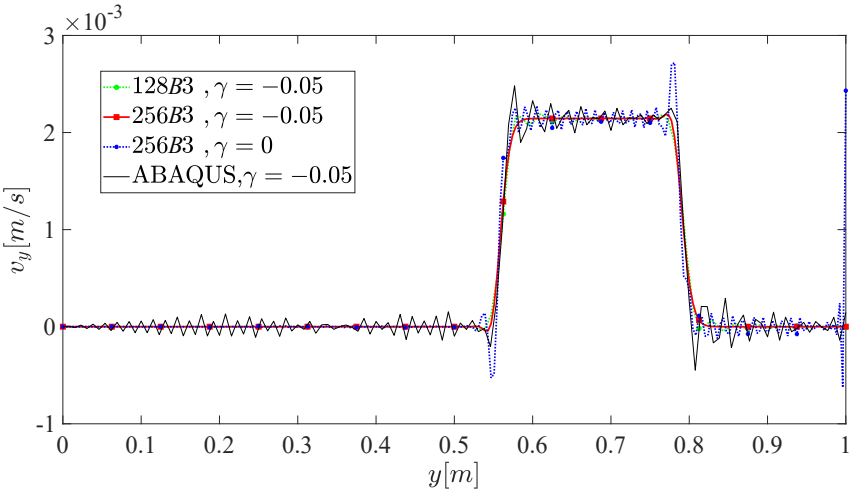

(c) $t = 3.0 \times 10^{-4}$ s

Figure 15: Through-the-length variation of v_y at $(x, y, z) = (b, :, h/2)$.

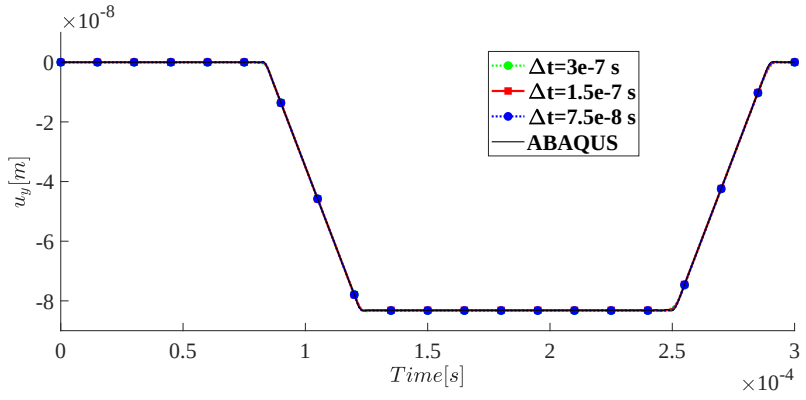

(a) u_y

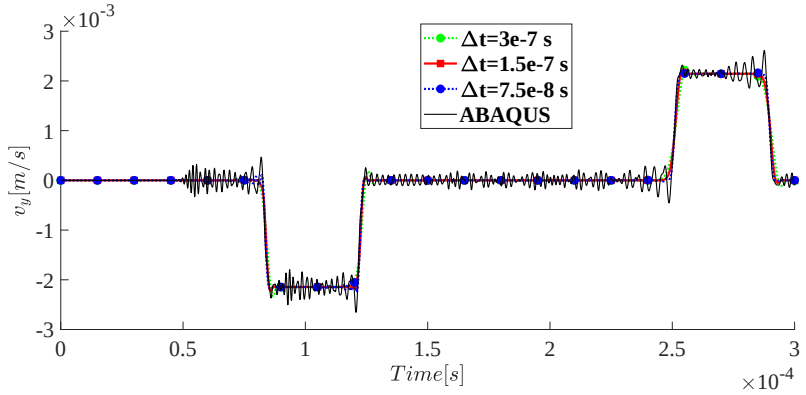

(b) v_y

Figure 16: Time history of two variables at point A for various time steps.

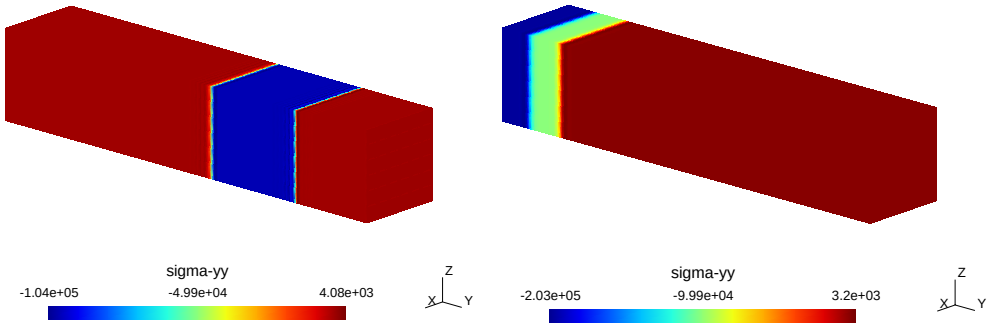

(a) $t = 7.2 \times 10^{-5}$ s

(b) $t = 1.8 \times 10^{-4}$ s

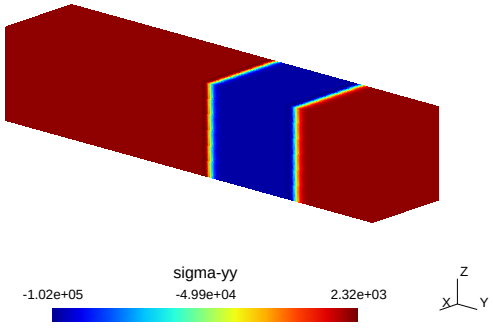

(c) $t = 3.0 \times 10^{-4}$ s

Figure 17: 3D contour plot of stress (σ_{yy}) wave propagation.

ing higher frequency components can be dissipated and the oscillation behaviour will be eliminated to a great extent. Therefore, the increase of the order of the elements makes sense instead of the reduction of the time step counterpart.

Fig. 17 shows the 3D plot of σ_{yy} at three typical times. From this figure, we can understand the propagation process better with special attention to the interactions between the incident wave and reflected wave. The minimum value at $t = 1.8 \times 10^{-4}$ s is more or less twice that of the other two times.

6.3.3 A metallic beam subjected to a moving load

Figure 18: A metallic beam under the moving load.

To test the applicability of the proposed models on the structure under the moving load condition, we consider a simply supported aluminum beam with the following geometric sizes and material properties: length $L = 10$ m, width $b = 0.4$ m, height $h = 0.5$ m; Young modulus $E = 72.4$ GPa, Poisson ratio $\nu = 0.33$, material density $\rho = 2770$ kg/m^3. The load can be perceived as a line load over the entire width which travels along the y-axis direction on the upper surface. The explicit formulation is given as: $p(t) = p_0 \times \delta(y - v_y t)$ with p_0 equal to 1250 N/m, constant velocity v_y equal to 40 m/s and $\delta(.)$ is the Dirac function, as shown in Fig. 18. The analytical solution of u_z is derived based on the Euler-Bernoulli beam model from Tao et al. [68], which can be written as:

$$u_z = \sum_{i=1}^{\Delta} \frac{2p_0}{I_0} \frac{1}{\left(i\pi v_y\right)^2 - \omega_i^2} \left(sin\frac{i\pi v_y}{L} t - \frac{i\pi v_y}{L\omega_i} sin\omega_i t \right) sin\frac{i\pi}{L} t \tag{27}$$

where $\omega_i = \left(\frac{i\pi}{L}\right)^2 \sqrt{\frac{Eh^2}{12\rho}}$.

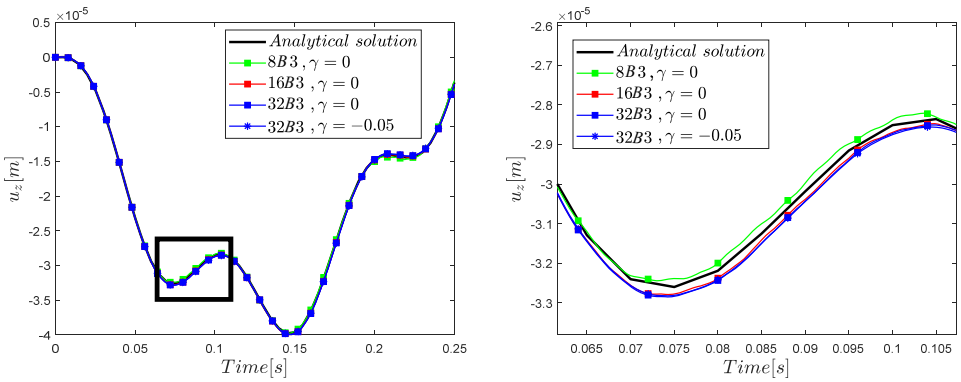

Figure 19: The mid-span displacement-time curve for different numbers of elements and γ.

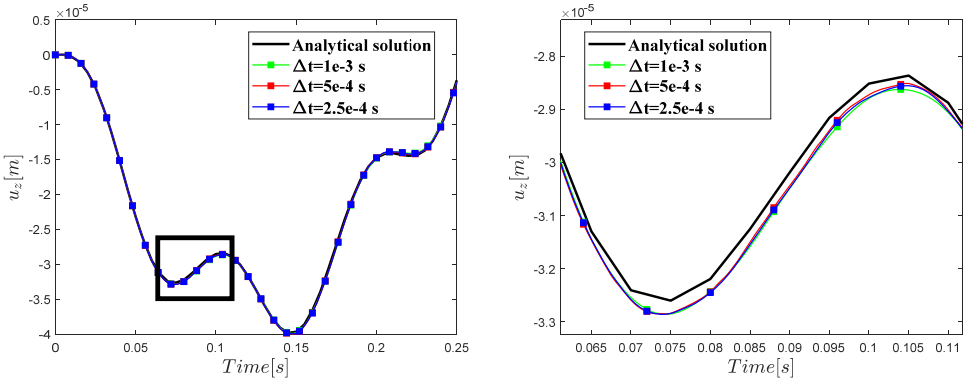

Figure 20: The mid-span displacement-time curve for different time steps with 16B3.

Fig. 19 and 20 show the graphs of the mid-span u_z against the time considering different numbers of elements, time steps and parameters γ. It is shown that the time step and parameter γ factors have a negligible effect on the solutions, reaching the desired values gradually with 16B3 model.

6.3.4 A composite beam subjected to a moving load

In the last section, further study is extended to the case of a two-layer laminated beam subjected to a moving load. The geometric shape is the same as that in the previous case. Its material properties are listed in Table 4. An antisymmetric $[-15°/15°]$ lamination scheme is taken into account. The structure is clamped at both ends and subjected to a moving pressure on the upper surface, which can be expressed as:$p(t) = p_0 \times sin(\omega t) \times \delta(y - v_y t)$ with p_0 equal to 1250 N/m, constant velocity v_y equal to 10 m/s and excitation frequency ω equal to 10 rad/s.

Table 4: Material properties

E_L	E_T, E_Z	$\nu_{LT}, \nu_{LZ}, \nu_{TZ}$	G_{LT}, G_{LZ}	G_{TZ}
250.0 GPa	10.0 GPa	0.25	5.0 GPa	2.0 GPa

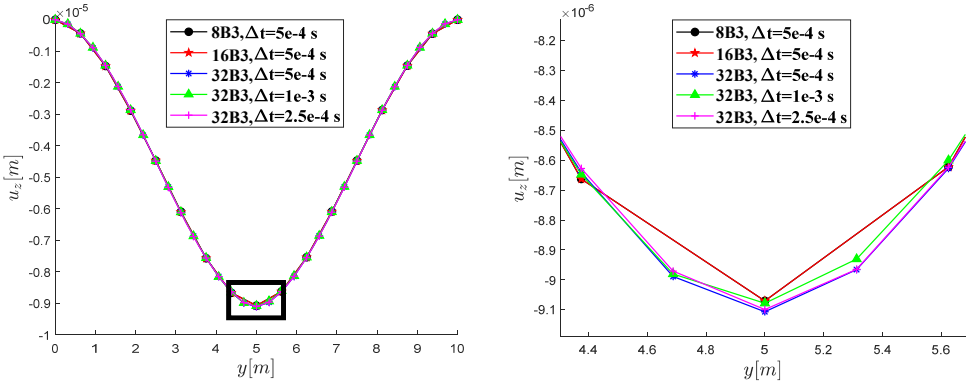

Figure 21: The variation of u_z along the line $(x, y, z) = (b, :, 0)$ at $t = 0.125$ s.

Fig. 21 analyzes the effect of the number of elements and the time step on the u_z distribution along the y-axis at $t = 0.125$ s. It can be concluded that 8B3, 16B3 and $\Delta t = 1.0 \times 10^{-3}$ perform marginally worse than other models.

Enabling a tradeoff between the accuracy and computational cost, 32B3, together with $\Delta t = 5.0 \times 10^{-4}$ is selected in the subsequent analysis.

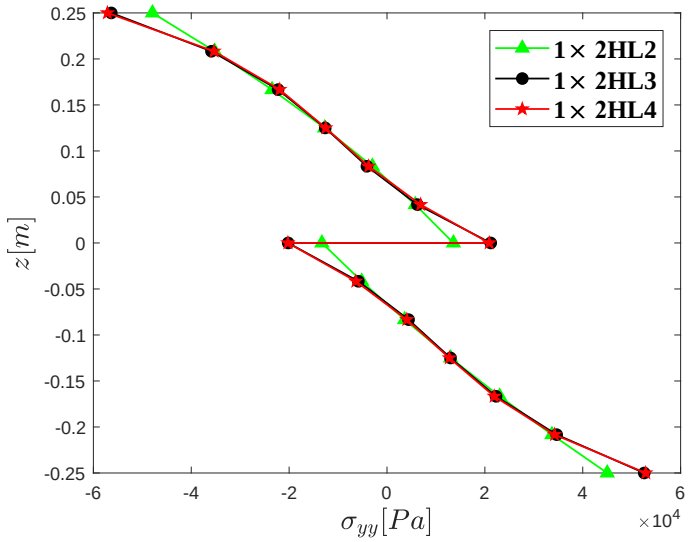

Figure 22: Through-the-thickness variation of of σ_{yy} at $t = 0.125$ s with 32B3.

Fig. 22 shows the through-the-thickness distribution of σ_{yy} on the line $(x, y, z) = (b/2, L/2, :)$ at $t = 0.125$ s. The convergent results can be obtained by a gradual degree elevation of cross-section kinematics, leading to the determination of 1×2HL3 in the following analysis straightforwardly.

The parametric study is a necessary step in the structural design. In the light of this factor, great efforts are devoted to study the effect of the fiber orientation angle, moving velocity and excitation frequency on the maximum dynamic deflection (u_z^{max}) at point $(x, y, z) = (b/2, L/2, 0)$ under two different boundary conditions, as shown in Fig. 23. The results in Fig. 23(a) indicate that u_z^{max} increases with a growing number of the fiber orientation angle, being more prominent for the hinged-hinged boundary condition. In Fig. 23(b), the approximate parabolic variation of u_z^{max} versus the excitation frequency is depicted for both boundary conditions. Obviously, excitation frequencies of extreme values ($\omega \approx 70 rad/s$ for "Hinged-Hinged" and $\omega \approx 165 rad/s$ for "Clamped-Clamped") are in the vicinity of natural frequencies of the structure, thus causing results with larger values. On the other hand, the variation of u_z^{max} can be divided into two stages. In the first stage, before the excitation frequency reaches 120 rad/s, the hinged-hinged boundary condition leads to larger u_z^{max}, while in the second stage, the trend is reversed. In Fig. 23(c), u_z^{max} converges to the same value monotonously with the increase of the moving velocity except for a slight drop in the initial stage.

7 Conclusions

This paper develops a computational framework of geometrically linear isogeometric analysis for solving the weak-form governing equations based on 1D refined beam models. The resulting model is used to solve static, free vibration and dynamic problems of beam structures. The Carrera Unified Formulation (CUF) is used to construct the hierarchical beam model. In the framework of CUF, the cross-section kinematics are defined using hierarchical

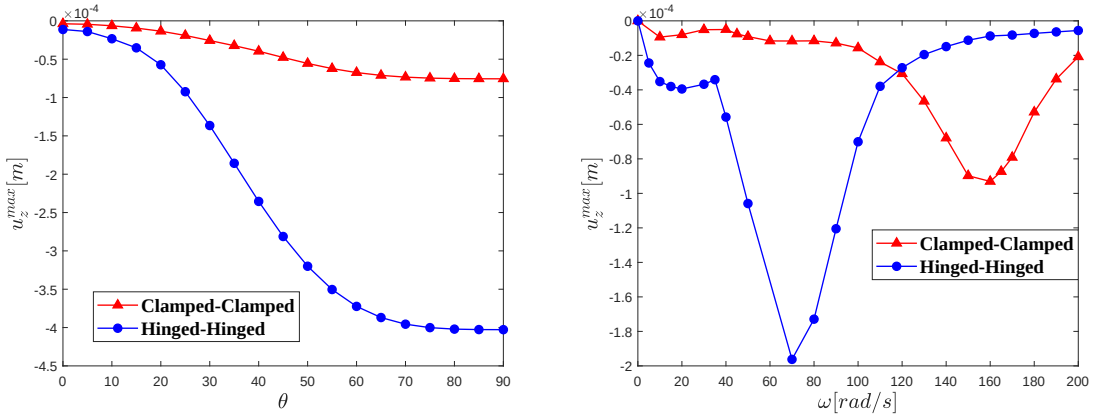

(a) Fiber orientation angle

(b) Excitation frequency

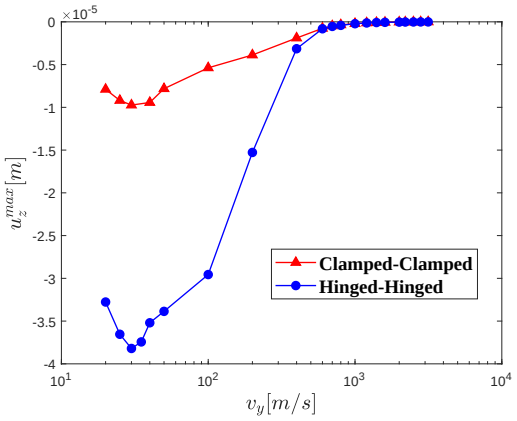

(c) Moving velocity

Figure 23: The parametric study.

Legendre polynomials, thus obtaining a Layer-wise description of the section without making any ad hoc assumptions. The generalized displacements in the axial domain are interpolated through B-spline functions. Subsequently, the weak-form governing equations are derived via the principle of virtual work. This kind of models can improve the numerical accuracy over various mechanical problems. Through the numerical investigation of beam-like structures, composed of isotropic or anisotropic material properties, the following conclusions can be drawn:

1. For the static problem, IGA 1D CUF-HLE can guarantee the continuity of the displacements, strains and stresses along the axial direction. This phenomenon is more prominent in the detection of the shear stress, which exhibits oscillatory behaviors obtained by FEM 1D CUF-HLE.

2. For the free vibration problem, IGA 1D CUF-HLE can reach a compromise between the computational efficiency and accuracy in the simulation of non-classical modes, which cannot be attained in 3D FEM. Moreover, as regards natural frequencies a narrow frequency spectrum, HLE models with higher-order expansions and more expansional sub-domains are recommended.

3. For the dynamic problem, the time steps and element numbers are two key factors, having an influence on the results at different times with varying degree. Particularly, in the process of stress wave propagation, the lack of enough elements both in IGA 1D CUF-HLE and 3D FEM will give rise to non-negligible spurious oscillations and numerical dispersion errors in terms of the stress and velocity variables. Besides, IGA 1D CUF-HLE with an appropriate γ value can overcome this drawback perfectly, while 3D FEM with the same γ value should increase the element continuously to fulfill similar inhibitive effect.

Although in this first development only straight beams are considered, the validity and generality of the method are not compromised. Further extensions of the model will deal with the analysis of curved geometries, for instance making use of the Frenet-Serret reference frame, as in [69]. Besides, more complex nonlinear problems, e.g., large displacements and rotations can be completed using a total Lagrangian approach [70].

Acknowledgments

The first author acknowledges the support by the scholarship from the Politecnico di Torino (Grant No. 1225/2017 and 1939/2018).

APPENDIX A Fundamental nucleus

3×3 fundamental nucleus of the stiffness matrix are defined as:

$$
\begin{aligned}
K^{\tau sij}_{e(11)} = \;& J_{i,_y j} \triangleleft F_\tau C_{46} F_{s,_z} \triangleright + J_{i,_y j} \triangleleft F_\tau C_{26} F_{s,_x} \triangleright + J_{i,_y j,_y} \triangleleft F_\tau C_{66} F_s \triangleright + \\
& J_{ij} \triangleleft F_{\tau,_z} C_{44} F_{s,_z} \triangleright + J_{ij} \triangleleft F_{\tau,_z} C_{24} F_{s,_x} \triangleright + J_{ij,_y} \triangleleft F_{\tau,_z} C_{46} F_s \triangleright + \\
& J_{ij,_y} \triangleleft F_{\tau,_x} C_{26} F_s \triangleright + J_{ij} \triangleleft F_{\tau,_x} C_{24} F_{s,_z} \triangleright + J_{ij} \triangleleft F_{\tau,_x} C_{22} F_{s,_x} \triangleright \\
K^{\tau sij}_{e(12)} = \;& J_{i,_y j} \triangleleft F_\tau C_{66} F_{s,_x} \triangleright + J_{i,_y j} \triangleleft F_\tau C_{56} F_{s,_z} \triangleright + J_{i,_y j,_y} \triangleleft F_\tau C_{36} F_s \triangleright + \\
& J_{ij} \triangleleft F_{\tau,_x} C_{26} F_{s,_x} \triangleright + J_{ij} \triangleleft F_{\tau,_x} C_{25} F_{s,_z} \triangleright + J_{ij} \triangleleft F_{\tau,_z} C_{46} F_{s,_x} \triangleright + \\
& J_{ij} \triangleleft F_{\tau,_z} C_{45} F_{s,_z} \triangleright + J_{ij,_y} \triangleleft F_{\tau,_z} C_{34} F_s \triangleright + J_{ij,_y} \triangleleft F_{\tau,_x} C_{23} F_s \triangleright \\
K^{\tau sij}_{e(13)} = \;& J_{i,_y j} \triangleleft F_\tau C_{46} F_{s,_x} \triangleright + J_{i,_y j} \triangleleft F_\tau C_{16} F_{s,_z} \triangleright + J_{i,_y j,_y} \triangleleft F_\tau C_{56} F_s \triangleright + \\
& J_{ij} \triangleleft F_{\tau,_z} C_{44} F_{s,_x} \triangleright + J_{ij} \triangleleft F_{\tau,_z} C_{14} F_{s,_z} \triangleright + J_{ij} \triangleleft F_{\tau,_x} C_{24} F_{s,_x} \triangleright + \\
& J_{ij} \triangleleft F_{\tau,_x} C_{12} F_{s,_z} \triangleright + J_{ij,_y} \triangleleft F_{\tau,_z} C_{45} F_s \triangleright + J_{ij,_y} \triangleleft F_{\tau,_x} C_{25} F_s \triangleright \\
K^{\tau sij}_{e(21)} = \;& J_{ij,_y} \triangleleft F_{\tau,_x} C_{66} F_s \triangleright + J_{ij,_y} \triangleleft F_{\tau,_z} C_{56} F_s \triangleright + J_{i,_y j} \triangleleft F_\tau C_{34} F_{s,_z} \triangleright + \\
& J_{i,_y j} \triangleleft F_\tau C_{23} F_{s,_x} \triangleright + J_{i,_y j,_y} \triangleleft F_\tau C_{36} F_s \triangleright + J_{ij} \triangleleft F_{\tau,_x} C_{46} F_{s,_x} \triangleright + \\
& J_{ij} \triangleleft F_{\tau,_x} C_{26} F_{s,_x} \triangleright + J_{ij} \triangleleft F_{\tau,_z} C_{45} F_{s,_z} \triangleright + J_{ij} \triangleleft F_{\tau,_z} C_{25} F_{s,_x} \triangleright \\
K^{\tau sij}_{e(22)} = \;& J_{ij} \triangleleft F_{\tau,_x} C_{66} F_{s,_x} \triangleright + J_{ij} \triangleleft F_{\tau,_x} C_{56} F_{s,_z} \triangleright + J_{ij} \triangleleft F_{\tau,_z} C_{56} F_{s,_x} \triangleright + \\
& J_{ij} \triangleleft F_{\tau,_z} C_{55} F_{s,_z} \triangleright + J_{ij,_y} \triangleleft F_{\tau,_x} C_{36} F_s \triangleright + J_{ij,_y} \triangleleft F_{\tau,_z} C_{35} F_s \triangleright + \\
& J_{i,_y j} \triangleleft F_\tau C_{36} F_{s,_x} \triangleright + J_{i,_y j} \triangleleft F_\tau C_{35} F_{s,_z} \triangleright + J_{i,_y j,_y} \triangleleft F_\tau C_{33} F_s \triangleright \\
K^{\tau sij}_{e(23)} = \;& J_{ij} \triangleleft F_{\tau,_x} C_{46} F_{s,_x} \triangleright + J_{ij} \triangleleft F_{\tau,_x} C_{16} F_{s,_z} \triangleright + J_{ij} \triangleleft F_{\tau,_z} C_{45} F_{s,_x} \triangleright + \\
& J_{ij} \triangleleft F_{\tau,_z} C_{15} F_{s,_z} \triangleright + J_{ij,_y} \triangleleft F_{\tau,_x} C_{56} F_s \triangleright + J_{ij,_y} \triangleleft F_{\tau,_z} C_{55} F_s \triangleright + \\
& J_{i,_y j} \triangleleft F_\tau C_{34} F_{s,_x} \triangleright + J_{i,_y j} \triangleleft F_\tau C_{13} F_{s,_z} \triangleright + J_{i,_y j,_y} \triangleleft F_\tau C_{35} F_s \triangleright \\
K^{\tau sij}_{e(31)} = \;& J_{i,_y j} \triangleleft F_\tau C_{45} F_{s,_z} \triangleright + J_{i,_y j} \triangleleft F_\tau C_{25} F_{s,_x} \triangleright + J_{i,_y j,_y} \triangleleft F_\tau C_{56} F_s \triangleright + \\
& J_{ij} \triangleleft F_{\tau,_x} C_{44} F_{s,_z} \triangleright + J_{ij} \triangleleft F_{\tau,_x} C_{24} F_{s,_x} \triangleright + J_{ij} \triangleleft F_{\tau,_z} C_{12} F_{s,_x} \triangleright + \\
& J_{ij} \triangleleft F_{\tau,_z} C_{14} F_{s,_z} \triangleright + J_{ij,_y} \triangleleft F_{\tau,_x} C_{46} F_s \triangleright + J_{ij,_y} \triangleleft F_{\tau,_z} C_{16} F_s \triangleright \\
K^{\tau sij}_{e(32)} = \;& J_{i,_y j} \triangleleft F_\tau C_{56} F_{s,_x} \triangleright + J_{i,_y j} \triangleleft F_\tau C_{55} F_{s,_z} \triangleright + J_{i,_y j,_y} \triangleleft F_\tau C_{35} F_s \triangleright + \\
& J_{ij} \triangleleft F_{\tau,_z} C_{16} F_{s,_x} \triangleright + J_{ij} \triangleleft F_{\tau,_z} C_{15} F_{s,_z} \triangleright + J_{ij} \triangleleft F_{\tau,_x} C_{46} F_{s,_x} \triangleright + \\
& J_{ij} \triangleleft F_{\tau,_x} C_{45} F_{s,_z} \triangleright + J_{ij,_y} \triangleleft F_{\tau,_x} C_{34} F_s \triangleright + J_{ij,_y} \triangleleft F_{\tau,_z} C_{13} F_s \triangleright \\
K^{\tau sij}_{e(33)} = \;& J_{i,_y j} \triangleleft F_\tau C_{45} F_{s,_x} \triangleright + J_{i,_y j} \triangleleft F_\tau C_{15} F_{s,_z} \triangleright + J_{i,_y j,_y} \triangleleft F_\tau C_{55} F_s \triangleright + \\
& J_{ij} \triangleleft F_{\tau,_x} C_{44} F_{s,_x} \triangleright + J_{ij} \triangleleft F_{\tau,_x} C_{14} F_{s,_z} \triangleright + J_{ij} \triangleleft F_{\tau,_z} C_{14} F_{s,_x} \triangleright + \\
& J_{ij} \triangleleft F_{\tau,_z} C_{11} F_{s,_z} \triangleright + J_{ij,_y} \triangleleft F_{\tau,_x} C_{45} F_s \triangleright + J_{ij,_y} \triangleleft F_{\tau,_z} C_{15} F_s \triangleright
\end{aligned}
\tag{A.1}
$$

where $\triangleleft \cdot \triangleright = \int_\Omega \mathrm{d}\Omega$ is a cross-section moment parameter, whereas

$$
\begin{aligned}
J_{ij} &= \int_0^1 R_i^p R_j^p y_{,\xi}\, \mathrm{d}\xi, \quad J_{ij,_y} = \int_0^1 R_i^p R_{j,\xi}^p \mathrm{d}\xi \\
J_{i,_y j} &= \int_0^1 R_{i,\xi}^p R_j^p \mathrm{d}\xi, \quad J_{i,_y j,_y} = \int_0^1 R_{i,\xi}^p R_{j,\xi}^p / y_{,\xi}\, \mathrm{d}\xi
\end{aligned}
\tag{A.2}
$$

, and the suffix after the comma means the derivatives. It should be pointed out that the integration above is performed over the parametric space [0, 1]. In order to implement Gauss quadrature smoothly, the mathematical transformation of integration variables serves as an alternative tool, as elaborated in [48].

References

[1] W. A. Oldfather, C. A. Ellis, and D. M. Brown. Leonhard euler's elastic curves. *Isis*, 20(1):72–160, 1933.

[2] S. P. Timoshenko. On the correction for shear of the differential equation for transverse vibrations of prismatic bars. *Philosophical Magazine Series*, 41(245):744–746, 1921.

[3] O. C. Zienkiewicz and R. L. Taylor. *The finite element method for solid and structural mechanics*. Elsevier, 2005.

[4] B. A. Boley. On the accuracy of the bernoulli-euler theory for beams of variable section. *Journal of Applied Mechanics*, 30(3):373–378, 1963.

[5] R. Davis, R. D. Henshell, and G. B. Warburton. A timoshenko beam element. *Journal of Sound and Vibration*, 22(4):475–487, 1972.

[6] D. L. Thomas, J. M. Wilson, and R. R. Wilson. Timoshenko beam finite elements. *Journal of Sound and Vibration*, 31(3):315–330, 1973.

[7] J. Thomas and B. A. H. Abbas. Finite element model for dynamic analysis of timoshenko beam. *Journal of Sound and Vibration*, 41(3):291–299, 1975.

[8] J. R. Hutchinson. Transverse vibrations of beams, exact versus approximate solutions. *Journal of Applied Mechanics*, 48(4):923–928, 1981.

[9] T. R. Tauchert. On the validity of elementary bending theory for anisotropic elastic slabs. *Journal of Composite Materials*, 9(2):207–214, 1975.

[10] F. Gordaninejad and C. W. Bert. A new theory for bending of thick sandwich beams. *International Journal of Mechanical Sciences*, 31(11-12):925–934, 1989.

[11] M. Levinson. A new rectangular beam theory. *Journal of Sound and Vibration*, 74(1):81–87, 1981.

[12] M. Stein. Vibration of beams and plate strips with three-dimensional flexibility. *Journal of Applied Mechanics*, 56(1):228–231, 1989.

[13] T. Kant and B. S. Manjunatha. On accurate estimation of transverse stresses in multilayer laminates. *Computers and Structures*, 50(3):351–365, 1994.

[14] A. A. Khdeir and J. N. Reddy. Free vibration of cross-ply laminated beams with arbitrary boundary conditions. *International Journal of Engineering Science*, 32(12):1971–1980, 1994.

[15] M. Karama, K. S. Afaq, and S. Mistou. Mechanical behaviour of laminated composite beam by the new multi-layered laminated composite structures model with transverse shear stress continuity. *International Journal of Solids and Structures*, 40(6):1525–1546, 2003.

[16] A. S. Sayyad and Y. M. Ghugal. Bending, buckling and free vibration of laminated composite and sandwich beams: A critical review of literature. *Composite Structures*, 171:486–504, 2017.

[17] J. M. Davies and P. Leach. First-order generalised beam theory. *Journal of Constructional Steel Research*, 31(2-3):187–220, 1994.

[18] N. Silvestre and D. Camotim. Second-order generalised beam theory for arbitrary orthotropic materials. *Thin-Walled Structures*, 40(9):791–820, 2002.

[19] R. Schardt. Generalized beam theoryan adequate method for coupled stability problems. *Thin-Walled Structures*, 19(2-4):161–180, 1994.

[20] R. Bebiano, N. Silvestre, and D. Camotim. Local and global vibration of thin-walled members subjected to compression and non-uniform bending. *Journal of Sound and Vibration*, 315(3):509–535, 2008.

[21] R. Bebiano, D. Camotim, and N. Silvestre. Dynamic analysis of thin-walled members using generalised beam theory (gbt). *Thin-Walled Structures*, 72:188–205, 2013.

[22] El F. R. Non-uniform warping including the effects of torsion and shear forces. part i: A general beam theory. *International Journal of Solids and Structures*, 44(18-19):5912–5929, 2007.

[23] J. Wackerfuß and F. Gruttmann. A nonlinear hu–washizu variational formulation and related finite-element implementation for spatial beams with arbitrary moderate thick cross-sections. *Computer Methods in Applied Mechanics and Engineering*, 200(17-20):1671–1690, 2011.

[24] H. H. Chen and K. M. Hsiao. Coupled axial–torsional vibration of thin-walled z-section beam induced by boundary conditions. *Thin-Walled Structures*, 45(6):573–583, 2007.

[25] M. K. Ferradi, X. Cespedes, and M. Arquier. A higher order beam finite element with warping eigenmodes. *Engineering Structures*, 46:748–762, 2013.

[26] K. Yoon and P. S. Lee. Modeling the warping displacements for discontinuously varying arbitrary cross-section beams. *Computers and Structures*, 131:56–69, 2014.

[27] V. V. Volovoi, D. H. Hodges, V. L. Berdichevsky, and V. G. Sutyrin. Asymptotic theory for static behavior of elastic anisotropic i-beams. *International Journal of Solids and Structures*, 36(7):1017–1043, 1999.

[28] W. Yu, V. V. Volovoi, D. H. Hodges, and X. Hong. Validation of the variational asymptotic beam sectional analysis. *AIAA Journal*, 40(10):2105–2112, 2002.

[29] W. Yu and D. H. Hodges. Elasticity solutions versus asymptotic sectional analysis of homogeneous, isotropic, prismatic beams. *Journal of Applied Mechanics*, 71(1):15–23, 2004.

[30] E. Carrera. Theories and finite elements for multilayered plates and shells: a unified compact formulation with numerical assessment and benchmarking. *Archives of Computational Methods in Engineering*, 10(3):215–296, 2003.

[31] E. Carrera, G. Giunta, and M. Petrolo. *Beam structures: classical and advanced theories*. John Wiley & Sons, 2011.

[32] E. Carrera and G. Giunta. Refined beam theories based on a unified formulation. *International Journal of Applied Mechanics*, 2(01):117–143, 2010.

[33] M. Filippi, A. Pagani, M. Petrolo, G. Colonna, and E. Carrera. Static and free vibration analysis of laminated beams by refined theory based on chebyshev polynomials. *Composite Structures*, 132:1248–1259, 2015.

[34] E. Carrera and M. Petrolo. Refined beam elements with only displacement variables and plate/shell capabilities. *Meccanica*, 47(3):537–556, 2012.

[35] E. Carrera, A. G. De Miguel, and A. Pagani. Hierarchical theories of structures based on legendre polynomial expansions with finite element applications. *International Journal of Mechanical Sciences*, 120:286–300, 2017.

[36] E. Carrera, G. Giunta, P. Nali, and M. Petrolo. Refined beam elements with arbitrary cross-section geometries. *Computers and Structures*, 88(5):283–293, 2010.

[37] E. Carrera, M. Petrolo, and P. Nali. Unified formulation applied to free vibrations finite element analysis of beams with arbitrary section. *Shock and Vibration*, 18(3):485–502, 2011.

[38] A. Catapano, G. Giunta, S. Belouettar, and E. Carrera. Static analysis of laminated beams via a unified formulation. *Composite Structures*, 94(1):75–83, 2011.

[39] E. Carrera, M. Filippi, P. K. R. Mahato, and A. Pagani. Advanced models for free vibration analysis of laminated beams with compact and thin-walled open/closed sections. *Journal of Composite Materials*, 49(17):2085–2101, 2015.

[40] A. Pagani, A. G. De Miguel, M. Petrolo, and E. Carrera. Analysis of laminated beams via unified formulation and legendre polynomial expansions. *Composite Structures*, 156:78–92, 2016.

[41] M. Petrolo, I. Kaleel, G. De Pietro, and E. Carrera. Wave propagation in compact, thin-walled, layered, and heterogeneous structures using variable kinematics finite elements. *International Journal for Computational Methods in Engineering Science and Mechanics*, 19(3):207–220, 2018.

[42] M. Dan, A. Pagani, and E. Carrera. Free vibration analysis of simply supported beams with solid and thin-walled cross-sections using higher-order theories based on displacement variables. *Thin-Walled Structures*, 98:478–495, 2016.

[43] Y. Yan, A. Pagani, and E. Carrera. Exact solutions for free vibration analysis of laminated, box and sandwich beams by refined layer-wise theory. *Composite Structures*, 175:28–45, 2017.

[44] A. Pagani, Y. Yan, and E. Carrera. Exact solutions for static analysis of laminated, box and sandwich beams by refined layer-wise theory. *Composites Part B: Engineering*, 131:62–75, 2017.

[45] Y. Yan, A. Pagani, E. Carrera, and Q. W. Ren. Exact solutions for the macro-, meso-and micro-scale analysis of composite laminates and sandwich structures. *Journal of Composite Materials*, 52(22):3109–3124, 2018.

[46] A. Pagani, E. Carrera, M. Boscolo, and J. R. Banerjee. Refined dynamic stiffness elements applied to free vibration analysis of generally laminated composite beams with arbitrary boundary conditions. *Composite Structures*, 110:305–316, 2014.

[47] T. J. R. Hughes, J. A Cottrell, and Y. Bazilevs. Isogeometric analysis: Cad, finite elements, nurbs, exact geometry and mesh refinement. *Computer Methods in Applied Mechanics and Engineering*, 194(39-41):4135–4195, 2005.

[48] J. A. Cottrell, T. J. R. Hughes, and Y. Bazilevs. *Isogeometric analysis: toward integration of CAD and FEA*. John Wiley & Sons, 2009.

[49] J. Kiendl, F. Auricchio, T. J. R. Hughes, and A. Reali. Single-variable formulations and isogeometric discretizations for shear deformable beams. *Computer Methods in Applied Mechanics and Engineering*, 284:988–1004, 2015.

[50] J. A. Cottrell, A. Reali, Y. Bazilevs, and T. J. R. Hughes. Isogeometric analysis of structural vibrations. *Computer Methods in Applied Mechanics and Engineering*, 195(41-43):5257–5296, 2006.

[51] J. A. Cottrell, T. J. R. Hughes, and A. Reali. Studies of refinement and continuity in isogeometric structural analysis. *Computer Methods in Applied Mechanics and Engineering*, 196(41-44):4160–4183, 2007.

[52] W. B. Wen, S. Y. Duan, K. Wei, Y. B. Ma, and D. N. Fang. A quadratic b-spline based isogeometric analysis of transient wave propagation problems with implicit time integration method. *Applied Mathematical Modelling*, 59:115–131, 2018.

[53] Vuong N. Van D., T. H. Ong, and C. H. Thai. Dynamic responses of euler–bernoulli beam subjected to moving vehicles using isogeometric approach. *Applied Mathematical Modelling*, 51:405–428, 2017.

[54] A. T. Luu, N. I. Kim, and J. Lee. Isogeometric vibration analysis of free-form timoshenko curved beams. *Meccanica*, 50(1):169–187, 2015.

[55] F. Maurin, L. Dedè, and A. Spadoni. Isogeometric rotation-free analysis of planar extensible-elastica for static and dynamic applications. *Nonlinear Dynamics*, 81(1-2):77–96, 2015.

[56] A. Kefal, K. A. Hasim, and M. Yildiz. A novel isogeometric beam element based on mixed form of refined zigzag theory for thick sandwich and multilayered composite beams. *Composites Part B: Engineering*, 167:100–121, 2019.

[57] M. Lezgy-Nazargah, P. Vidal, and O. Polit. Nurbs-based isogeometric analysis of laminated composite beams using refined sinus model. *European Journal of Mechanics-A/Solids*, 53:34–47, 2015.

[58] T. T. Yu, S. S. Yin, T. Q. Bui, S. F. Xia, S. Tanaka, and S. Hirose. Nurbs-based isogeometric analysis of buckling and free vibration problems for laminated composites plates with complicated cutouts using a new simple fsdt theory and level set method. *Thin-Walled Structures*, 101:141–156, 2016.

[59] Y. J. Guo, A. P. Nagy, and Z. Gürdal. A layerwise theory for laminated composites in the framework of isogeometric analysis. *Composite Structures*, 107:447–457, 2014.

[60] A. Alesadi, M. Galehdari, and S. Shojaee. Free vibration and buckling analysis of composite laminated plates using layerwise models based on isogeometric approach and carrera unified formulation. *Mechanics of Advanced Materials and Structures*, 25(12):1018–1032, 2018.

[61] A. Alesadi, M. Galehdari, and S. Shojaee. Free vibration and buckling analysis of cross-ply laminated composite plates using carrera's unified formulation based on isogeometric approach. *Computers and Structures*, 183:38–47, 2017.

[62] A. Alesadi, S. Ghazanfari, and S. Shojaee. B-spline finite element approach for the analysis of thin-walled beam structures based on 1d refined theories using carrera unified formulation. *Thin-Walled Structures*, 130:313–320, 2018.

[63] E. Carrera and M. Petrolo. Refined one-dimensional formulations for laminated structure analysis. *AIAA Journal*, 50(1):176–189, 2012.

[64] B. Szabó, A. Düster, and E. Rank. The p-version of the finite element method. *Encyclopedia of Computational Mechanics*, 2004.

[65] Y. Yan, E. Carrera, A. G. Miguel, A. Pagani, and Q. W. Ren. Meshless analysis of metallic and composite beam structures by advanced hierarchical models with layer-wise capabilities. *Composite Structures*, 2018.

[66] J. N. Reddy. *Mechanics of laminated composite plates and shells: theory and analysis*. CRC press, 2004.

[67] H. M. Hilber and T. J. R. Hughes. Collocation, dissipation and [overshoot] for time integration schemes in structural dynamics. *Earthquake Engineering and Structural Dynamics*, 6(1):99–117, 1978.

[68] C. Tao, Y. M. Fu, and H. L. Dai. Nonlinear dynamic analysis of fiber metal laminated beams subjected to moving loads in thermal environment. *Composite Structures*, 140:410–416, 2016.

[69] A. G. de Miguel, G. De Pietro, E. Carrera, G. Giunta, and A. Pagani. Locking-free curved elements with refined kinematics for the analysis of composite structures. *Computer Methods in Applied Mechanics and Engineering*, 337:481–500, 2018.

[70] A. Pagani and E. Carrera. Unified formulation of geometrically nonlinear refined beam theories. *Mechanics of Advanced Materials and Structures*, 25(1):15–31, 2018.